5-2013

Fabrication and Characterization of Si(1-x)Ge(x) Semiconductor Alloy for Sensor Applications

Daniel Aaron Schaeffer
University of Tennessee - Knoxville, dschaef2@utk.edu

To the Graduate Council:

I am submitting herewith a thesis written by Daniel Aaron Schaeffer entitled "Fabrication and Characterization of Si(1-x)Ge(x) Semiconductor Alloy for Sensor Applications." I have examined the final electronic copy of this thesis for form and content and recommend that it be accepted in partial fulfillment of the requirements for the degree of Master of Science, with a major in Materials Science and Engineering.

Philip D. Rack, Major Professor

We have read this thesis and recommend its acceptance:

Thomas T. Meek, Syed K. Islam

Accepted for the Council:
Dixie L. Thompson

Vice Provost and Dean of the Graduate School

(Original signatures are on file with official student records.)

Fabrication and Characterization of $Si_{1-x}Ge_x$ Semiconductor Alloy for Sensor Applications

A Thesis Presented for
the Master of Science
Degree
The University of Tennessee, Knoxville

Daniel Aaron Schaeffer
May 2013

Acknowledgements

I would like to thank my advisor Dr. Philip D. Rack for his support on this project and continuous motivation along with Dr. Matthew Lassiter for mentoring and training me in various aspects of sample preparation, characterization, fabrication, and testing. I would also like to thank Dr. Boyd Evans for taking the time to work closely with me and giving valuable advice on clean room techniques and procedures. In addition, I thank all the people at the Center for Nanophase Materials and Science (CNMS) and Oak Ridge National Laboratory (ORNL) for their support. Lastly and most importantly I would like to thank all my family, especially my wife for her understanding, love, and support.

Abstract

$Si_{1-x}Ge_x$ [Si(1-x)Ge(x)] semiconductor alloys have emerged as materials with many important applications in the electronic industry due to its tunable electronic, optical, and physical properties. It has been studied and analyzed for the fabrication of high-speed micro electronics (e.g., SiGe heterojunction bipolar transistors (HBT) and high electron mobility field effect transistors) and thermo-photovoltaics (e.g., photodetectors, solar cells, thermoelectric power generators and temperature sensors). Other applications of $Si_{1-x}Ge_x$ include tunable neutron and x-ray monochromators and γ-ray [gamma-ray] detectors. In these applications, the $Si_{1-x}Ge_x$ alloy is generally used in the form of epilayers that have to be deposited on a lattice-matched substrate (wafer). Therefore $Si_{1-x}Ge_x$ bulk single crystals with a specific composition (x) are needed for the extraction of such wafers.

Amorphous silicon made by plasma decomposition of silane (SiH_4) usually has high resistivity and good photoconductivity with low optical absorption; however, investigations establish a-Si as a semiconductor of lower electrical conductivity than crystalline Si with a large number of unpaired crystal-surface-like electrons distributed throughout the bulk of a-Si. It has also been shown that films sputtered in an argonhydrogen atmosphere exhibit similar properties[1]. In addition, a-Si produced by sputtering in a pure argon atmosphere has low resistivity, poor photoconductivity, and high optical absorption below 1.5 eV. By co-sputtering silicon and germanium in a pure

argon atmosphere in an ultra-low vacuum (≥ [greater than or equal to] 10^7 [10^7] torr) the semiconductor quality can be greatly enhanced with capabilities of using the Si1-xGex alloy for near infrared (NIR) photosensor applications.

This thesis presents an experimental study for RF sputter deposited thin films of compositionally varying a-SiGe on Si/SiO_2 [silicon/silicon dioxide] wafers of ~200 nm film thickness that are thermally annealed to induce uniform crystallization. The goal is to develop a NIR optical sensor with high efficiency and good thermal stability. As-deposited and annealed wafers were characterized by using Energy Dispersive X-ray analysis (EDX) for composition analysis, X-ray diffraction (XRD) for microstructural characterization, Raman spectroscopy for structural and compositional analysis, and electrical probe measurements.

Dedication

I dedicate this thesis to my wife, Ashley, for all her help, love, and support.

Table of Contents

List of Tables

List of Figures

1. Introduction

1.1 Motivation and Background

Nature, over several billions of years of evolution by natural selection, has presented itself as an amazing system in a constant trend of optimization. From a macroscopic scale down to molecular level biological structures, it has exhibited some very interesting properties. Studies from systematically ordered matter in a nano- and micrometer scale in electronic and optical systems have always been of great technological and scientific significance. One such revolution is based on the organization and control of matter on the nanometer scale to obtain optimized results on the macroscopic level.

Solid-state physics is one area of scientific research that has directly benefitted from the revolution of an understanding the nanometer scale in order to manipulate and characterize bulk materials. Solid-state physics is the study of rigid matter, or solids, through methods such as quantum mechanics, crystallography, electromagnetism, and metallurgy. This area of research is generally interested in how the large-scale properties of solid materials result from their atomic-scale properties.

Solid-state materials can be classified into three groups: insulators, semiconductors, and conductors and each one can be defined loosely by its intrinsic resistivity. Insulators are materials typically having an electrical conductivity $\sigma \leq 10^{-8}$ S/cm; semiconductors have a conductivity in the range of 10^{-8} S/cm $< \sigma < 10^{3}$ S/cm; and conductors are materials with high conductivities, having $\sigma \geq 10^{3}$ S/cm. Alternatively,

semiconductors can be defined as a material whose energy gap lies in the range of 0 to about 3 eV. Thus, solid-state physics forms the theoretical basis of materials science and also has direct applications, for example in the technology of semiconductors.

Research on semiconducting materials started in the early nineteenth century and since then many semiconductors have been investigated. There are many minerals found in nature, such as zinc-blende (ZnS), cuprite (Cu2O) and galena (PbS), that are semiconductors while the most well known semiconductor is undoubtedly silicon (Si). Until as recently as the early 1960's though, germanium (Ge) was the most frequently employed semiconductor material; however, it was not ideal for applications requiring weak current consumption and/or operation under high temperatures. With the addition of two-, three-, or more element composite semiconductors synthesized within laboratories, the family of semiconductors forms one of the most robust and versatile class of materials available to man.

Semiconductor devices are now commonplace in just about every household, whether we realize it or not. In 2003, the semiconductor industry estimated about 90 million transistors manufactured each year for each person alive on the planet and rose to over one billion transistors per person by 2010 _ENREF_2. In the late 1940's, the invention of the transistor was the start of a rapid development towards increasingly faster and smaller electronic components, ranging from the simple and elegant to complex systems built with these components. These devices have influenced and/or enabled fiber-based optical communication, optical storage and high-frequency

amplification, photography, and lighting, along with many others, while making the technology economically feasible.

A careful analysis is required on the different semiconductors for the deposition, annealing, and lithographic processes. There are several physical properties of semiconductors that have to be understood before making the right choice for fabrication. The fundamental science of semiconductor technology and devices is nothing new or recent and research on the $Si_{1-x}Ge_x$ alloy system dates back to as early as 1954. The physics of semiconductor devices is naturally dependent on the physics of semiconductors themselves, and the ways we understand materials is constantly changing. Consequently, it is important to understand the fundamental properties of the basis materials.

A silicon (germanium) atom in the silicon (germanium) crystal forms four tetrahedrally oriented, covalent bonds with four neighbors, and the repetition of this exact bonding geometry with a well-defined bond length and angle leads to the diamond cubic structure. Amorphous silicon and germanium have been the subjects of many investigations[2] and crystalline silicon and germanium have been thoroughly characterized and relatively well-understood properties. However, it is difficult to define uniquely the properties of the amorphous materials. For example, the electrical resistivities vary with time and annealing histories. Even if allowance for annealing is made, inconsistencies between laboratories are abundant in the literature.[3,4,5,6]

The $Si_{1-x}Ge_x$ alloy offers very promising material features such that the band structure and thus the effective mass and mobility of both electrons and holes are

significantly affected by alloy composition, temperature, and strain. Therefore, the electrical and optical properties of this material can be tailored according to the needs of device applications. Furthermore, other very important aspects of $Si_{1-x}Ge_x$ alloy are its ease of integration with the well-developed and long-existing silicon technology and its low-cost production compared to III-V group (and other) semiconductor materials.

Due to the sophisticated growth techniques that, for decades, have been and continue to be improved, semiconductors are an ideal choice for the electronics industry. Laboratory grown single crystals of Si and Ge can be grown with considerably higher thermal conductivity and fewer impurities than that of naturally occurring Si and Ge. Techniques such as Molecular Beam Epitaxy (MBE) and Metal-Organic Chemical Vapor Deposition (MOCVD) allow a single crystal to be formed with unparalleled precision, depositing one layer at a time.

In this work, SiGe sensors were fabricated using a co-sputtering process onto various substrates and followed by annealing to thermally induce crystallization and lithographic processes. Much work as been done in the area of fabrication and optimization of semiconductors for sensor and detector applications. Light dependent resistors (LDR) or photo resistors, are semiconductor devices that change resistance under illumination. These devices have many applications in industrial controls: item counters, presence and proximity sensors, flame detectors, photometric devices, etc.[7] Telecommunications is very important in our society today and much research is aimed towards improving performance of such IR detectors and sensors[8,9]. Prototype detector structures have been fabricated on Si substrates with GeSn as the active material for near-

IR telecommunications[10] with other near-IR detection and imaging based on poly-Ge photodiode arrays[11]. Silicon-based nanowires have been grown in a Au-Si system[12] and Au/Cr/Si microcantilevers are under current investigation[13]. Thermal annealing to crystallize as-deposited a-SiGe thin films has recently been reported for fabrication of a hydrogen gas sensor[14]. Comparisons have even been made between different a-Si thin film structures for use as image sensors for office automation and facsimile transmission[15]. Relatively recent use of hydrogenated binary alloys of Si with Ge, Sn, C, and N in devices such as solar cells[16,17,18,19] and light-emitting diodes[20,21,22] has motivated a great deal of research on the electronic properties of these materials.

The applications for Si, Ge and its variable compositional alloy $Si_{1-x}Ge_x$ have many possibilities and this thesis will demonstrate how it can be applied for a photoresitive sensor.

1.2 Organization of Thesis

This thesis has five chapters. The first chapter is a general introduction so SiGe semiconductor materials and applications. For subsequent chapters, a review is given in the introduction of each chapter referencing the related work.

The second chapter discusses general properties of semiconductors, focusing on silicon and germanium both in amorphous and crystalline form and is intended as a summary of materials properties as a basis of understanding applicable device characteristics. An overview of the structural, thermal, and physical properties are given with the relevant energy-band, carrier distribution/concentration, and transport properties.

The third chapter discusses the experimental procedures and fabrication process of the $Si_{1-x}Ge_x$ alloy and photoresistor devices. The fabrication of the alloy involves a deposition of the material onto a substrate and an annealing procedure to produce a crystalline form of the alloy. The as-deposited and annealed films are characterized via EDX, XRD, spectroscopic reflectometry, and Raman spectroscopy and a relationship is established between the annealing parameters (temperature and duration) and crystallinity. Finally, the device processing procedure is described and the electrical and photo-electrical measurements are described.

The fourth chapter presents the results obtained and gives a discussion on the photo and thermal response of the sensor and compares them to the optothermal behavior of similarly fabricated structures (sensors). Analyzing the I-V curves of the patterned electrodes helped in the characterization of the photoconductivity and a relative intensity measurement.

The fifth and final chapter concludes the thesis by summarizing the research and briefly discusses the potential of future applications given the various results and the outlook of future work relating to SiGe sensors.

2. Basic Properties of $Si_{1-x}Ge_x$ Alloy

This chapter provides basic information on the crystal structure (or lattice structure – including lattice parameters, equilibrium phase diagram, and electronic band structure), thermal, and physical properties of the $Si_{1-x}Ge_x$ solid solution as it forms the basis for understanding the forthcoming discussions concerning fabrication and device applications of $Si_{1-x}Ge_x$ systems.

2.1 Structure of $Si_{1-x}Ge_x$

2.1.1 Crystal (Lattice) Parameters

By basic intuition, visualizing a low-energy electron traveling through a solid crystal would seem nearly impossible without constant scattering as the atoms in crystals are packed so tightly that their centers are only a few angstroms apart. In addition, their diameters are small so that the scattering atoms are large relative to their spacing and one would only expect a mean free path between collisions to be on the order of only a few angstroms. Nonetheless, free electrons are able to travel through perfect crystals with relative ease allowing crystalline materials to conduct current efficiently.

The lattice structure of a crystal is formed by the periodic reoccurrence of a unit cell in three dimensional space, which is defined as the smallest building block of the crystal, so the unit cell completely describes the lattice structure. Thus, to visualize the lattice structure of a crystal, it is adequate to examine the unit cell of the crystal.

Silicon and germanium both belong to the IV-group of the periodic table. These two elements and their mixture crystallize with the diamond cubic lattice structure under atmospheric pressure. The diamond lattice structure is a generic name, which

characterizes all crystals crystallizing in the same pattern as diamond, and belongs to the cubic-crystal family. The arrangement of atoms in the diamond unit cell is pictured in Fig. 2-1 for SiGe.

The diamond unit cell is a cubic structure with atoms at each corner and at each face of the cube akin to the well-known face-centered cubic (fcc) cell. Unlike the fcc unit cell, the diamond cell hosts four additional interior atoms represented by the red-filled circles in Fig. 2-1. Each interior atom is located on one of the four body diagonals of the cube. All interior atoms are displaced one-quarter of the body diagonal with respect to associated corners along the corresponding diagonals. The numbers inside the circles within the diamond unit cell denote the height of the atoms with reference to base as a fraction of the cell dimension, denoted by a.

An alternative and easier way of visualizing the diamond space lattice might be to consider a lattice formed by the interpenetration of two fcc unit cells. Namely, the second fcc unit cell is displaced a quarter of the body diagonal relative to the first cell along the diagonal direction. In this case, the corner and face atoms of the diamond unit cell can be viewed as if they belong to the first fcc unit cell, whereas atoms of the diamond unit cell can be viewed as if they belong to the second fcc cell.

As each unit cell is brought adjacent to each other in the crystal, then each cell contains one-eight of each corner atom ($8 \times 1/8$) and one-half of each face atom ($6 \times 1/2$). Therefore, with four interior atoms, each diamond unit cell contains eight complete atoms.

As discussed, each atom in the unit cell is covalently bonded with its four equidistant nearest neighbors forming a tetrahedral structure as illustrated by a dashed box in the interior of the diamond unit cell in Fig 2-1a and is schematically represented in Fig. 2-2 for a two-dimensional plane. At low temperatures, the electrons are bound in their respective tetrahedron lattice and consequently they are not available for conduction. At higher temperatures, thermal vibrations may break covalent bonds resulting in a free or conduction electron that can participate in current conduction. The void or vacancy left by the free electron may be replaced by another free electron that results in a shift of this vacancy from one location to another moving in a direction opposite that of conduction electrons known as holes.

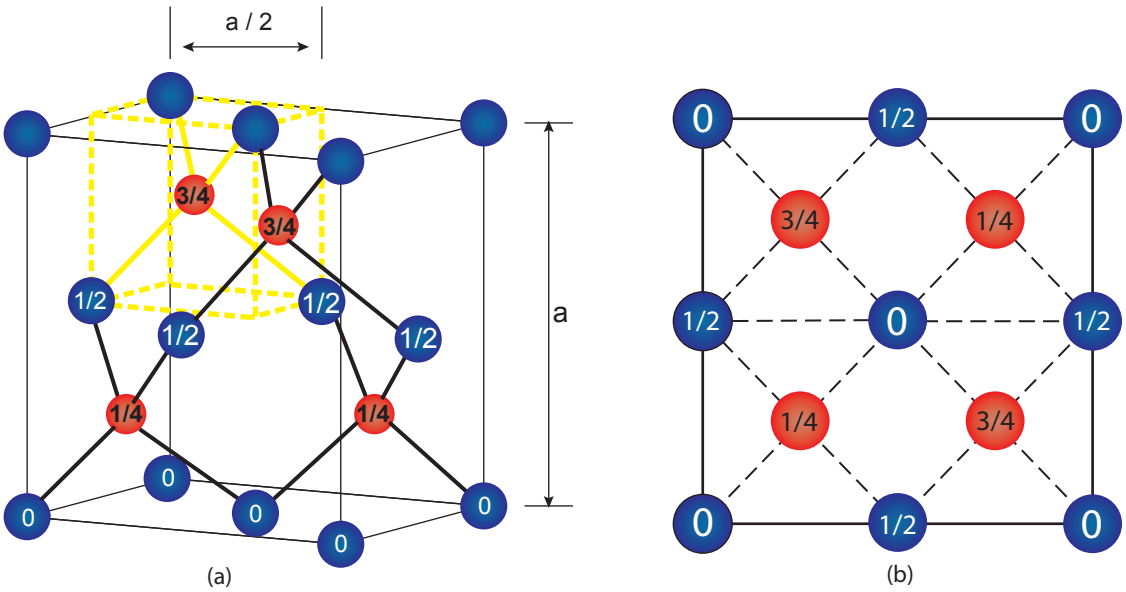

Figure 2-1 The sketch of the diamond unit cell (a) and projections of the cube face (b) with numbers indicating displacements of atoms normal to the base of the unit cell. Si atoms are represented by blue circles and Ge atoms by red circles.

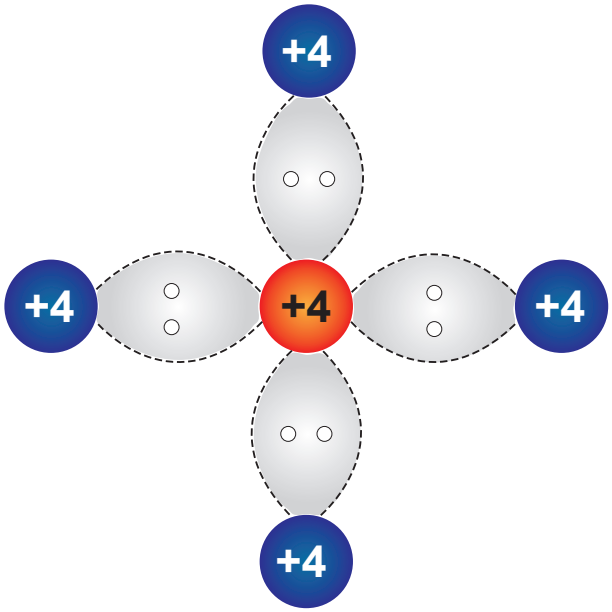

Figure 2-2 Two-dimensional schematic representation of a tetrahedron bond. Each atom has four electrons in the outer orbit and each atom shares these valence electrons with its four neighbors.

2.1.2 Equilibrium Phase Diagram

The equilibrium phase diagram for $Si_{1-x}Ge_x$ system (see Fig. 2.3) consists of three distinct regions, namely the upper region describing the liquid state, the lower region describing the solid state and an intermediate region where the solid and liquid states coexist. The curves that separate intermediate region of the phase diagram from the liquid state and solid state are called the liquidus and solidus curve, respectively. The region between the liquidus and solidus curves is usually referred to as the miscibility gap.

Silicon and germanium have complete solubility in each other both in solid and liquid states over the entire composition range as can be seen from the equilibrium phase diagram (see Fig. 2-3). Upon solidification, the mixture of silicon and germanium forms a substitutional solid solution. For a given composition and temperature in the phase diagram, the concentration of the silicon in the liquid and solid states can be determined by drawing a tie-line intercepting with the liquidus and solidus line at a given temperature. It can easily be noticed from the phase diagram that the concentration of silicon in the solid is always higher than the concentrations in liquid state. This implies that silicon solidifies faster since the melting temperature is higher than that of germanium.

The solidification process of the $Si_{1-x}Ge_x$ system can be explained by the illustration indicated on the representative $Si_{1-x}Ge_x$ phase diagram given in Fig. 2-4. When an arbitrary alloy with composition X_0 is cooled from the liquid state, denoted L, to a lower temperature, labeled T_1, the formation process of a solid solution begins. The composition of the first solidified solid solution can be obtained by extending the

temperature line (T_1) to the solidus curve and by drawing a vertical line from the intersection of the two lines to the composition axis. In this case, the composition of the first solidified solid solution is labeled x_{S1} and its arbitrary value is obviously greater than that of the initial melt.

Continuing the solidification process by decreasing the temperature to T_2, the composition of solid crystal (at the solidus line) shifts to x_{S2} due to the fact that silicon is preferentially consumed during crystal formation. The melt of the arbitrary alloy of composition X_0 now has the composition of x_{L2} and x_{S2}, demonstrating that germanium is increasing in both the solid and liquid phases. This is due to germanium atoms remaining in the liquid phase and a decrease in silicon concentration during crystal formation due to preferential consumption resulting in varying compositions throughout the solidification process.

The extent of the compositional non-homogeneity, or segregation, in a solidified crystal depends on the location (x) in the phase diagram where the alloy is solidified. The segregation is characterized by a coefficient k_0 that is known as the equilibrium segregation coefficient[23,24] and is defined as the ratio of the concentration of the solute in the solid, c_s, to that in the liquid, c_l, at the solid-liquid interface, or explicitly $k_0 = c_s/c_l$, and is a function of temperature. If k_0 is close to unity the alloy is known to be of a contemporary melting temperature.

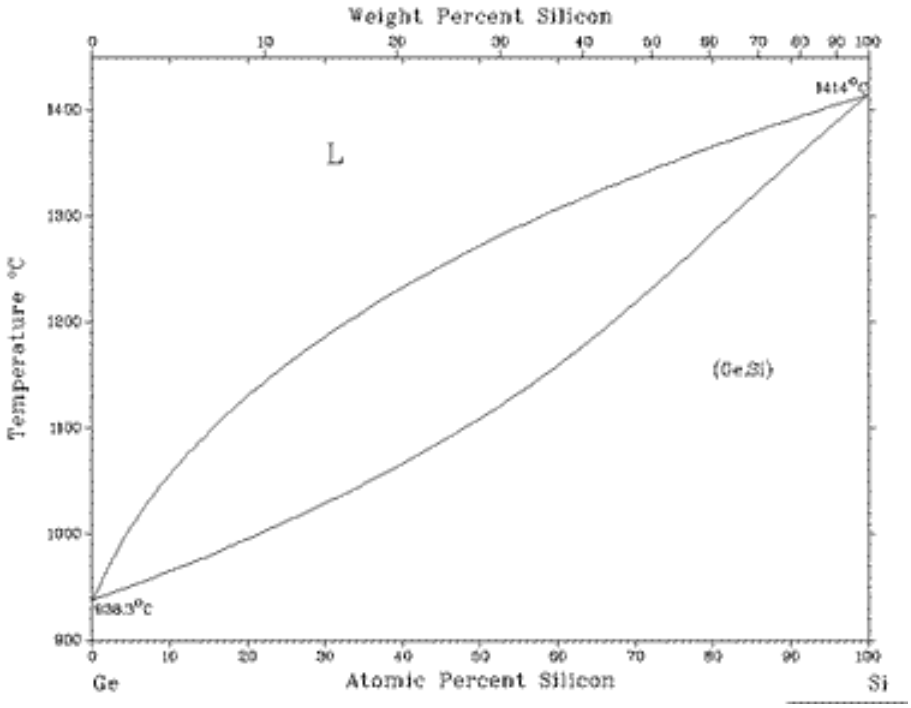

Figure 2-3 Equilibrium phase diagram of $Si_{1-x}Ge_x$ system

For the $Si_{1-x}Ge_x$ alloy system, k_0 values can be far from unity. For germanium-rich alloys, k_0 is bigger than unity and has values up to 5.5. For silicon-rich alloys, k_0 varies between one and about 0.3. Since the segregation coefficient is further away from unity for germanium rich-alloys than for silicon-rich alloys, it is easier to obtain a single crystal of a uniform composition from the silicon-rich side of the phase diagram. Also, $Si_{1-x}Ge_x$ is a good example for an alloy system having a strong tendency towards the formation of a composition gradient along the solidification direction due to the large miscibility gap between the solid and liquid phases and the large difference in melting temperatures. For this thesis, three compositions have been selected, all of which are in the silicon-rich regime.

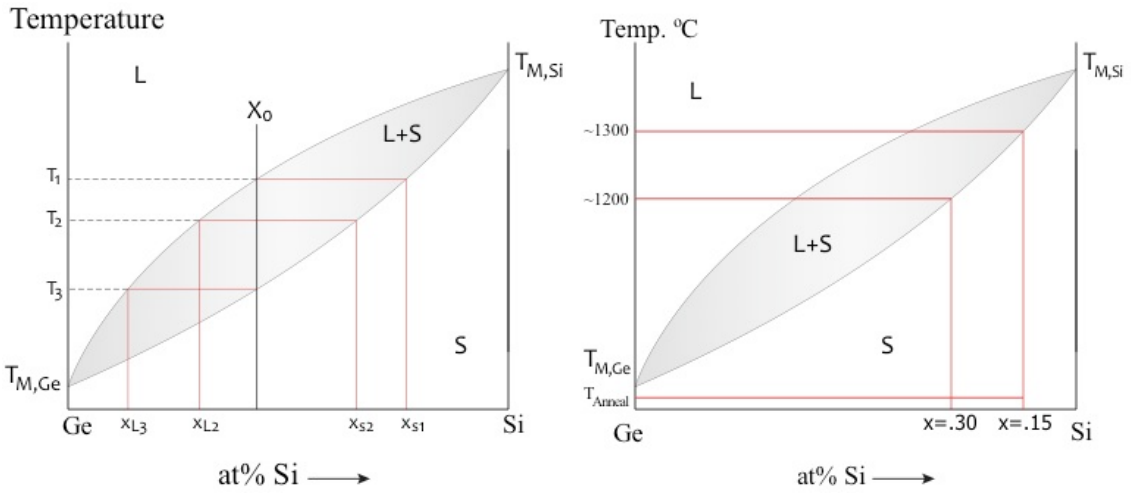

Figure 2-4 Representative phase diagram of $Si_{1-x}Ge_x$ illustrating solidification process and melting temperature comparison

2.1.3 Electronic Band Structure

For any isolated atom, the electrons of that atom will obey the laws of quantum mechanics and can only have discrete energy levels. The simplest model of this is given using an isolated hydrogen atom and the energy levels are described by the well know Bohr model[25,26] and is given as

$$E_H = -\frac{Z^2 m_0 e^4}{8\varepsilon_0^2 h^2 n^2} = -\frac{13.6}{n^2}\,\text{eV} \tag{1}$$

where m_0 is the free electron mass, e is the electronic charge, ε_0 is the free space permittivity, h is Planck's constant, and n is a positive integer.

Considering any two identical atoms, when they are far apart the allowed energy levels for a given quantum state (number) will be equal (i.e., two hydrogen atoms with E_H = -13.6 eV for n = 1). When the two arbitrary atoms come in close proximity with each other the quantized energy levels hybridize and will split into two levels or orbitals due to

the atomic interactions and since, according to the Pauli exclusion principle, each state can only contain one electron. This model can be expanded to three atoms brought together that generate three separate molecular orbital states.

This argument can be extended to the formation of a solid by bringing N atoms from an infinite distance in an infinite number of directions closer together until they reach the equilibrium inter-atomic distance, d. When the atoms come together to form a crystal, the N-fold degenerate energy level split into N separate but closely spaced levels creating a seemingly continuous band of energy.

Applying this to the case of silicon or germanium atoms arranged in a periodic lattice, initially with a very large lattice parameter – or interatomic distance – in order to first consider each atom as isolated particle coming from infinity. Figure 2-5 shows the formation of these bands as a function of the interatomic distance.

Each isolated atom has its discrete energy levels with the two levels with the highest energy labeled E_1 and E_2. As the interatomic spacing decreases, each degenerate energy level splits and begin to form energy bands. As the spacing continues to decrease the bands originating from different discrete levels lose their identities and merge together forming a single band. Approaching the equilibrium interatomic distance – which gives a lattice spacing of 5.43 Å for silicon and 5.65 Å for germanium – this continuous band again splits into two energy bands. These two continuous bands are known as the conduction band (CB) and the valence band (VB) and are separated by a forbidden region or gap known as the bandgap, E_g. The bandgap width is characteristic of the material itself and is temperature dependent.

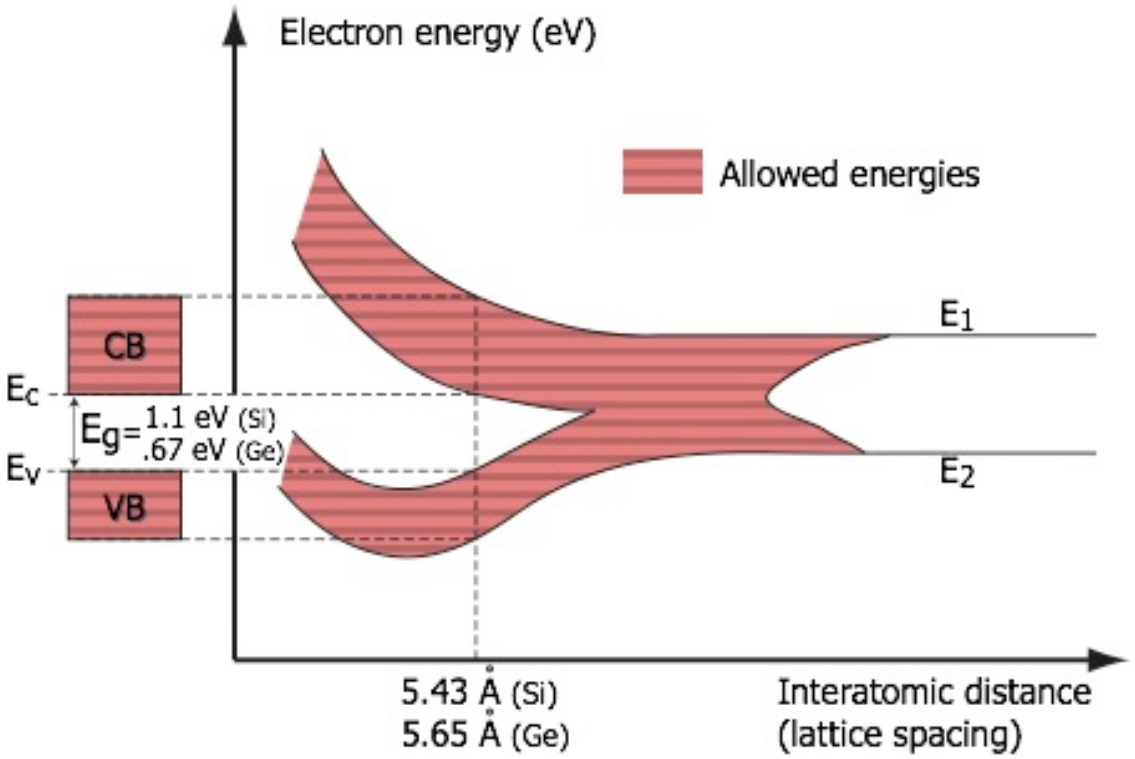

Figure 2-5 Band energy formation for electrons in a silicon crystal with a diamond lattice structure

The relation of the electron and hole energies is illustrated on the left side of Fig. 2-5. As discussed above, the separation between the energy of the lowest conduction band and the highest valence band is called the bandgap, E_g, which is a very important property for semiconductor materials. The bottom of the conduction band is designated E_C and corresponds to the potential energy of an electron, meaning the energy of a free electron at rest (no electric field). The kinetic energy is measured upward from E_C. Likewise, the top of the valence band is designated E_V and corresponds to the potential energy of the hole as the kinetic energy is measured downward from E_V.

Band structure is more complex than what is represented in Fig. 2-5. SiGe alloys are in the category of indirect band gap semiconductors, like their constituents (see Fig 2-

6). In pure silicon and germanium, the maximum in the valence band occurs at the center of the E vs $k = p/\hbar$ diagram where $k = 0$, whereas the minimum in the conduction band is located at $k \neq 0$[27]. Here, k is the wave number (also known for this application as crystal momentum), p is the momentum, and $\hbar$ is the modified Plank's constant.

For silicon and germanium, the conduction band minima occur along the <100> and <111> crystallographic directions, respectively. Therefore, when an electron transitions from the VB to the CB, a change in crystal momentum is required in addition to the change in energy, ΔE. A result of this indirect interaction between an electron and the energy bands is a significant effect on the optical properties of semiconductors. Consequently, indirect band gap semiconductors do not show as good optical properties as direct band gap semiconductors.

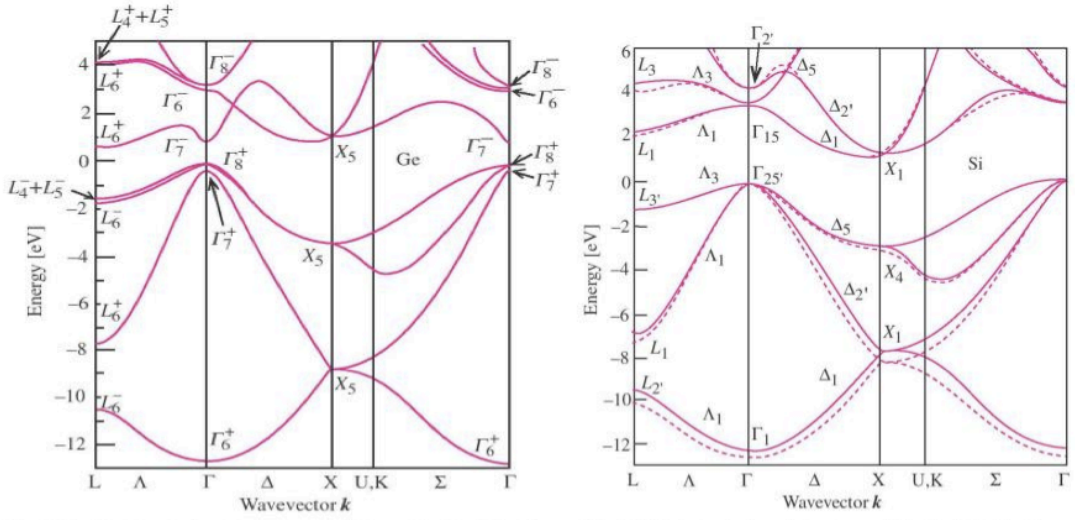

Figure 2-6 Electronic band structure of Ge (left) and Si (right). The energy at the top of the filled valence bands has been taken to be zero. Both Ge and Si are an indirect semiconductor because the maximum of the valence band (at Γ) does not coincide with the minimum of the conduction band (to the left at X)

2.2 Physical Properties of $Si_{1-x}Ge_x$

2.2.1 Band Gap Formation

There exists a relation[28] between the variation of the energy gap of semiconductors, E_g, and a given temperature, T such that

$$E_g = E_0 - \alpha T^2/(T+\beta) \tag{2}$$

where E_0 is the band gap energy at 0 K and α and β are constants. This equation, known as the Varshni equation, is based upon two main assumptions: that the energy gap should be proportional to T at moderate to high temperatures and proportional to T^2 at low temperatures.

The mechanism that contributes most to the change in energy gap with temperature is electron-lattice interactions, which are temperature dependent, that cause the positions of the conduction and valence bands to shift relative to each other. This leads to a dependence of temperature such that

$$T \ll \theta_D;\ \Delta E_g \propto T^2 \tag{3a}$$

$$T \gg \theta_D;\ \Delta E_g \propto T \tag{3b}$$

where θ_D is the Debye temperature. The constant β is approximated to be of the same order as the Debye temperature and experiment shows that this assumption is reasonable.

Using Eq. (2) with the appropriate values for the coefficients α and β (see table 1), the band gap for Si and Ge can be calculated and is shown in Fig. 2-7. The calculated results fit well both with theory and experiment showing that the band gap energy, E_g, for Si and Ge at 300 K is 1.12 eV and 0.66 eV, respectively.

Table 1 The forbidden energy gap, E_0, at 0 K and coefficients α and β of the Varshni equation. The Debye temperature is also given

	E_0 (eV)	α 10^{-4} (eV K^{-1})	β (K)	θ_D (K)
Ge	0.7437 ± 0.001	4.774 ± 0.30	235 ± 40	374
Si	1.1700 ± 0.001	4.730 ± 0.25	636 ± 50	645

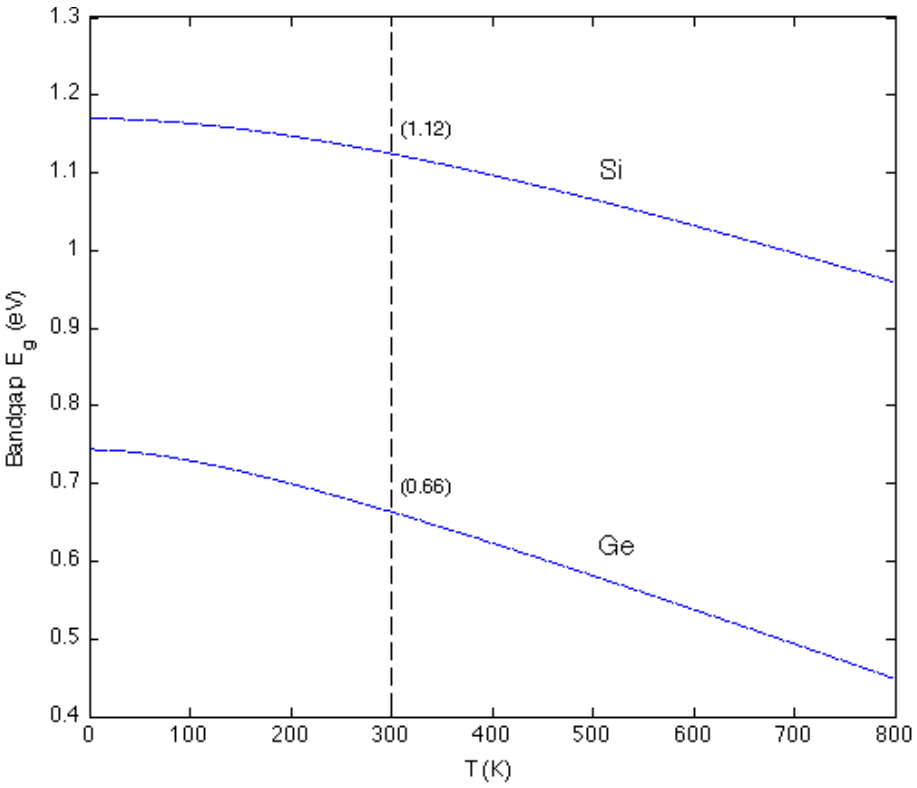

Figure 2-7 Band gap of Si and Ge as a function of temperature.

As a first principles approach, using a linear approximation in the form

$$f(x) = C_{Si}(1 - x) + C_{Ge}(x) \tag{4}$$

where C_{Si} is the band gap at T (K) for silicon, C_{Ge} is the band gap at T (K) for germanium, and x is the fractional composition of germanium expressed as a decimal, the

band gap for the compositional alloy $Si_{1-x}Ge_x$ can be found. Using this method one obtains a band gap energy at 300 K of 1.051 eV for $Si_{.85}Ge_{.15}$ and 0.982 eV for $Si_{.70}Ge_{.30}$.

As with the its elemental constituents the indirect band structure of $Si_{1-x}Ge_x$ alloy depends on temperature, however, it is also dependent upon composition. It has also been studied and observed _ENREF_27 that there is a sudden change in the slope of the band gap versus composition curve[29] occurring at ~ 15 at% Si. This abrupt change has been attributed to a switchover effect of the conduction band edge from the <100> minima characteristic of pure Si and Si-rich alloys to the <111> minima characteristic of pure Ge and Ge-rich alloys.

A portion of this curve is linear in the 0-15 at% Si region but the second portion of the curve is quadratic[27,30] in the remaining composition range. The analytical expressions are as follows _ENREF_28:

$$E_g^{<100>}(x) = 1.155 - 0.43x + 0.206x^2 \text{ eV} \quad (5a)$$

$$E_g^{<111>}(x) = 2.010 - 1.270x \text{ eV} \quad (5b)$$

where $E_g^{<100>}$ and $E_g^{<111>}$ represent the Si conduction band minima and the Ge conduction band minima, respectively, and x is the fractional composition of germanium expressed as a decimal.

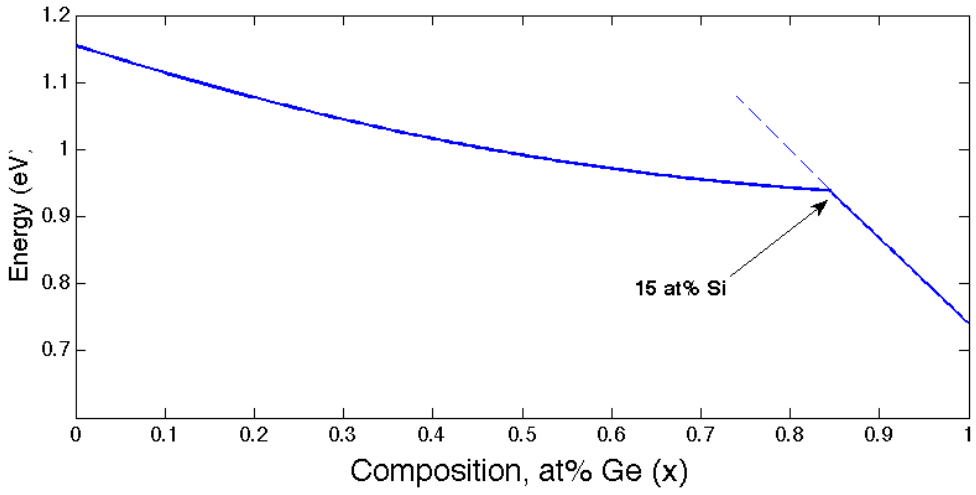

Figure 2-8 Band gap vs. composition, x, for $Si_{1-x}Ge_x$ alloys. The data is based off linear and quadratic equations determined from absorption measurements and low-temperature photoluminescence (PL) spectra.

The plotted results can be seen in Fig. 2-8. Using these equations we can estimate the anticipated compositional alloys band gap energies, which gives 1.095 eV for $Si_{.85}Ge_{.15}$ and 1.045 eV for $Si_{.70}Ge_{.30}$ and equates to a 4.03% and 5.98% deviation from the linear approximation.

2.2.2 Intrinsic Carrier Concentration

The thermal excitation of a carrier from the VB to the CB creates free carriers in both bands. The concentration of these carriers is called the intrinsic carrier concentration, denoted n_i. Semiconductor materials which have not been doped in order to change the carrier concentration are intrinsic materials. The intrinsic carrier concentration represents the number of electrons in the CB or the number of holes in the VB in intrinsic material. The number of carriers depends on the band gap and temperature. A large band gap will make it more difficult for a carrier to be thermally

excited across the band gap and therefore the intrinsic carrier concentration is lower in higher band gap materials.

The concentrations of electrons and holes in a pure semiconductor are equal and the intrinsic concentration is given by

$$n_i = 2\left(\frac{2\pi k}{h^2}\right)^{3/2} m^{*3/2}\, T^{3/2}\, exp\left(-\frac{E_g}{2kT}\right) \tag{6}$$

where the average density of states effective mass, m^*, is the geometric mean of the electron and hole density of states effective masses. That is

$$m^* = (m_n m_p)^{1/2} \tag{7}$$

where m_n and m_p are the effective electron and hole masses, respectively.

Since the values of E_g have been previously estimated using Eqs. (5a) and (5b) for $Si_{1-x}Ge_x$ and Eq. (2) for pure Si and Ge, the values of n_i can be calculated, assuming the value of m^* is known, which is a function of temperature, from Eq. (6). There have been abundant studies to obtain estimates of m^* and many n_i values obtained from using these effective masses were compared with Hall measurements. The best estimates are plotted in Fig. 2-9 along with interpolated data to estimate values for $Si_{1-x}Ge_x$. At 300 K, the accepted value of n_i for Si is 1.45×10^{10} cm^{-3} and for Ge is 2.4×10^{13} cm^{-3}. The values of n_i for $Si_{.85}Ge_{.15}$ and $Si_{.70}Ge_{.30}$ are 3.73×10^{11} cm^{-3} and 2.38×10^{12} cm^{-3}.

The inset in Fig. 2-9 shows the intrinsic carrier concentration plotted against reciprocal temperature to better show the dependence of carrier density as a function of

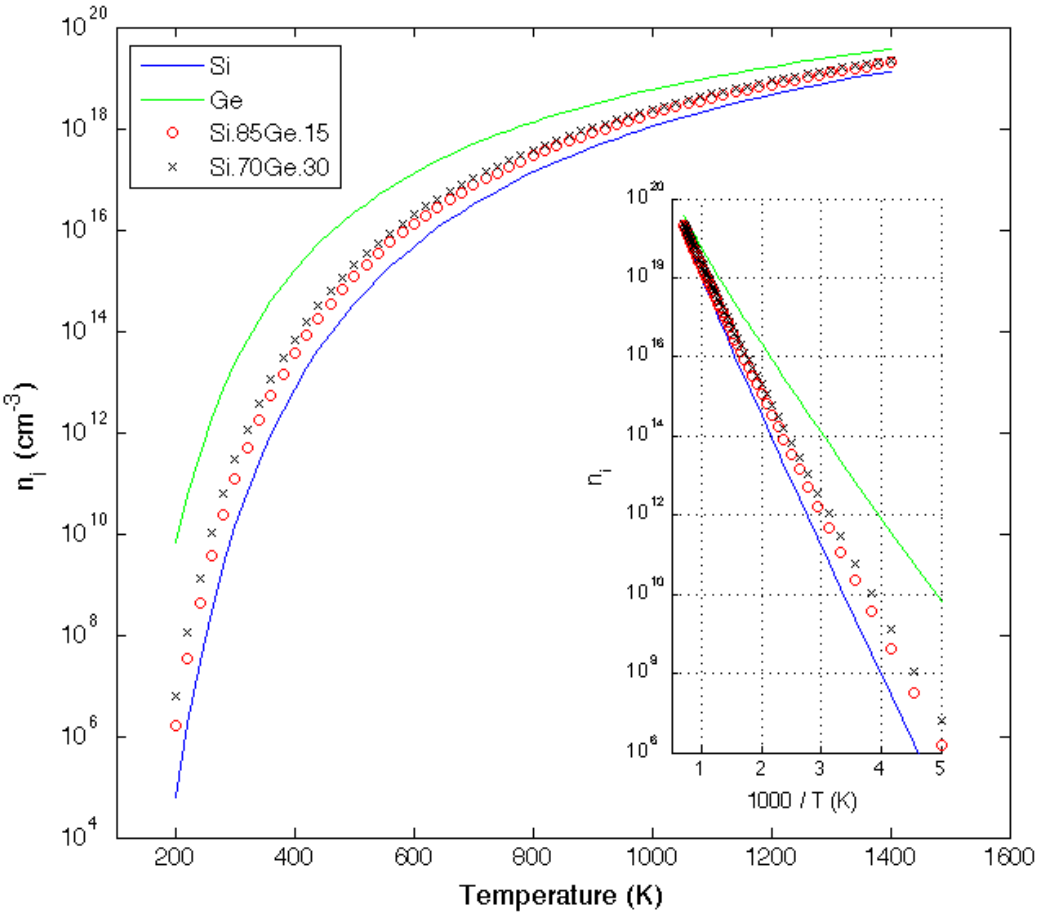

Figure 2-9 The intrinsic carrier concentration, n_i, as a function of T for Si, Ge and $Si_{1-x}Ge_x$. The inset shows the intrinsic carrier concentration as a function of reciprocal temperature on a log scale.

temperature. It can be seen in both plots that as the temperature becomes very high, that is close to the melting temperature, the carrier densities approach equality.

2.2.3 Carrier Transport

Electrons in the CB and holes in the VB are considered free carriers in the sense that they can move throughout the semiconductor lattice that makes up the crystal structure of the material. A simplistic but adequate description of carrier movement

portrays each carrier as moving in a random direction at a certain velocity (speed and direction).

The carrier moves in this random direction for a distance called the scattering length before colliding with a lattice atom. Once the collision takes place, the carrier moves away in a different random direction. The thermal velocity is the average carrier velocity. Carriers have a thermal velocity that is normally distributed around this average thermal velocity. Therefore, some carriers having a greater velocity and some lower.

Barring certain circumstances, there is no net movement of carriers in any direction. Each direction of carrier movement is equally probable, therefore the motion of a carrier in one direction will eventually be balanced by the movement of another carrier in the opposite direction.

After scattering off the lattice atoms, the carrier again moves in a random direction. Although carriers in a semiconductor are in constant random motion, there is no net motion of carriers unless there is a concentration gradient or an electric field.

2.3 Thermal and Optical Properties of $Si_{1-x}Ge_x$

2.3.1 Heat Capacity

The forbidden energy gap, or band gap, of a semiconductor is known to be a Gibbs energy, $G = H - TS$, which is the Gibbs energy of formation of electrons and holes[31,32,33]. Since the band gap, as a function of temperature, is the standard Gibbs energy for formation of electrons and holes as a function of temperature, the standard

enthalpy, entropy, and heat capacity can be calculated utilizing the following relationships[34]

$$\Delta E = \Delta H - T\Delta S \tag{8}$$

$$d\left(\frac{\Delta E}{T}\right)/d\left(\frac{1}{T}\right) = \Delta H = \Delta E - T\frac{d(\Delta E)}{dT} \tag{9}$$

$$\Delta C = \frac{d(\Delta \mathrm{H})}{\mathrm{dT}} = \mathrm{T}\frac{\mathrm{d}(\Delta \mathrm{S})}{\mathrm{dT}} \tag{10}$$

where $\Delta E = E_g - E_0$, ΔH is the enthalpy, ΔS is the entropy, and ΔC is the heat capacity.

The Varshni equation can be used to obtain the various thermodynamic functions at all temperatures up to the respective melting points. The heat capacity is of particular interest and can be obtained from Eq. (2) and the by determining the enthalpy. From Eq. (9) if follows that the gap enthalpy is

$$\Delta \mathrm{H(T)} = \Delta \mathrm{H(0)} + \alpha\beta\left(\frac{\mathrm{T}}{\mathrm{T}+\beta}\right)^2 \tag{11}$$

where α and β are constants from the Varshni equation. The heat capacity can now be determined by using Eq. (2) and Eq. (11)

$$\Delta \mathrm{C} = \frac{2\alpha\beta^2\mathrm{T}}{(\mathrm{T}+\beta)^2} \tag{12}$$

and is plotted in Fig. 2-10.

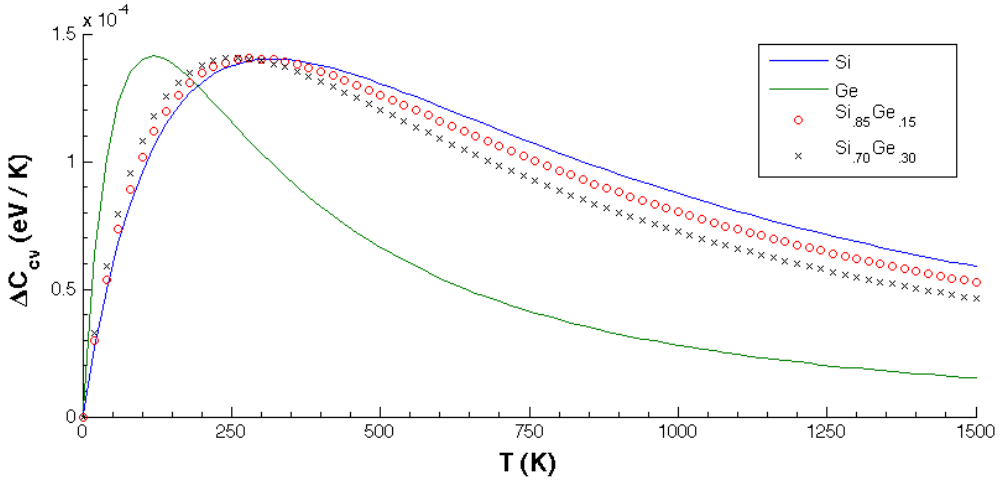

Figure 2-10 The heat capacity change, ΔC, for the formation of electrons and holes as a function of T for Si, Ge, and $Si_{1-x}Ge_x$

2.3.2 Optical Absorption

Photons incident on the surface of the $Si_{1-x}Ge_x$ semiconductor alloy will be reflected from the top surface, absorbed in the material by interaction with an electron, or, failing either of these two processes, will be transmitted through the material. For the $Si_{1-x}Ge_x$ photoresistor devices, reflection and transmission will typically be considered loss mechanisms as photons which are not absorbed do not create electron-hole pairs to contribute to the conductivity. If the photon is absorbed it has the possibility of exciting an electron from the valence band to the conduction band.

Photons from an arbitrary light source incident on the semiconductor material can be divided into three main groups based on their energy, E_{ph}, compared to that of the semiconductor band gap, E_g. If $E_{ph} < E_g$ then the photons interact only weakly with the semiconductor, passing through it as if it were transparent. This scenario will not be considered. If $E_{ph} = E_g$ then the photons have just enough energy to create an electron-hole pair and are efficiently absorbed. When $E_{ph} > E_g$ the photons can be strongly

absorbed. The photon energy greater than the band gap is, however, wasted as electrons quickly thermalize back down to the conduction band minima. The excess energy is dissipated heat that is distributed through the material by phonons (lattice vibrations) causing the band gap, since it is a function of temperature, to decrease as the temperature increase. These effects will also change the absorption coefficient.

The absorption coefficient determines how far into a material light of a particular wavelength can penetrate before it is absorbed. In a material with a low absorption coefficient, light is only poorly absorbed, and if the material is thin enough, as in the case of the thin film $Si_{1-x}Ge_x$ semiconductor, it will appear transparent to that wavelength. Typically semiconductor materials have a sharp edge in their absorption coefficient due to light that has energy below the band gap and therefore does not have sufficient energy to excite an electron into the conduction band from the valence bad. Consequently this light is not absorbed. The absorption coefficient, α, is defined using the following formula

$$\alpha = \frac{4\pi k}{\lambda} \tag{13}$$

where k is the extinction coefficient and λ is the wavelength in nm.

Even for photons that have an energy above the band gap the absorption coefficient is not constant but still depends strongly on wavelength. For photons which have an energy very close to that of the band gap, the absorption is still relatively low since the density of states near the VB and CB edge is low. As the photon energy increases, not just the electrons already having energy close to that of the band gap can interact with the photon. Therefore, a larger number of electrons can interact with the

photon and result in the photon being absorbed. However, as photon energy continues to increase the absorption coefficient (and therefore the absorption) will not continue to increase. This can be seen in Fig. 2-11 showing the absorption coefficient[35,36], α, for Si, Ge, and SiGe[27,37] _ENREF_34[38], _ENREF_25. The values for SiGe are based on a composition of 80 at% Si and 20 at% Ge. From the graph it is apparent that the maximum occurs near 4.4 eV, but it can also be seen that there is an edge like effect near 2 eV for Ge and 3 eV for Si and SiGe. These values at the maximum and band edge (3 eV) correspond to wavelengths of 282 nm for and 413 nm, respectively.

It can also be useful to plot the absorption coefficient as a function of wavelength. This plot is shown in Fig. 2-12. For infrared (IR) applications, Ge has a much higher absorption than Si, due to a lower band gap energy, and therefore Si-rich $Si_{1-x}Ge_x$ alloys are better suited for near IR (NIR) applications.

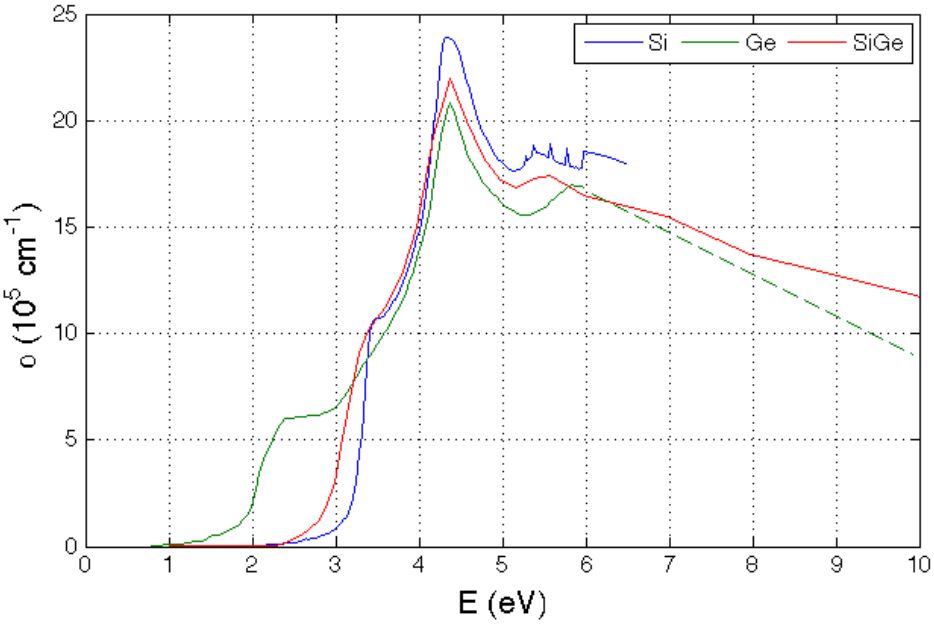

Figure 2-11 The absorption coefficient, α, in 10^5 cm^{-1} for the semiconductors Si, Ge and SiGe at 300 K as a function of photon energy. The dotted line for Ge is data that has been extrapolated for higher energy photons.

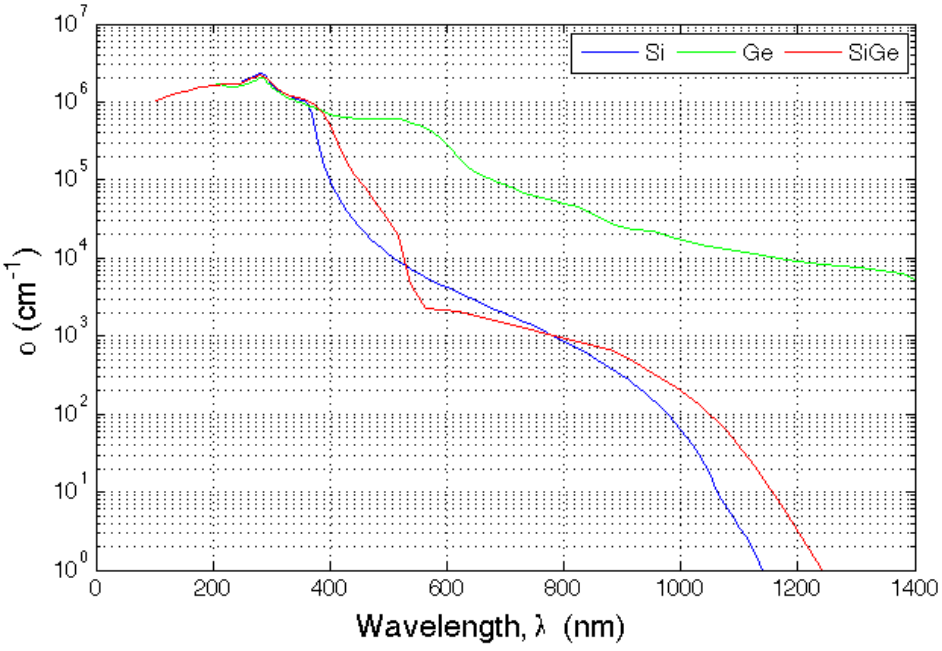

Figure 2-12 The absorption coefficient, α, in cm^{-1}, plotted against wavelength. Both Si and Ge are indirect bandgap semiconductors so there is a long tail in absorption, however Ge reaches further into the infrared region. Since the data is graphed on a log scale the drop in absorption at the band gap for Si (around 1100 nm) is sharper than might first appear.

3. Experimental Details

This chapter provides an in-depth discussion of the experimental procedures for sample preparation, including sputter deposition and thermally induced crystallization, testing/characterization, and device fabrication.

3.1 Deposition and Crystallization

3.1.1 Deposition of $Si_{1-x}Ge_x$

A radio frequency (RF) magnetron sputtering system (AJA International, Model ATC 2000) was used to deposit the amorphous $Si_{1-x}Ge_x$ thin films on 4 in. (100 mm), <100> p-type Si (B doped) wafers with 500 nm thermally-grown oxide layer. The sputtering targets consist of 2 in. diameter intrinsic germanium and silicon discs. All sputtering was carried out with an RF power of 200 W for the Si target, a gas flow of 25 standard cubic cm per minute (sccm), and a substrate bias of 150 V. The power for the Ge target was set to different values to control the amount of germanium in the films and vary the composition of the alloy. Deposition time varied with Ge power in an attempt to achieve a consistent film thickness, which range from 180 nm to 205 nm.

The background or base pressure was consistently kept at 6.5×10^{-4} mTorr (8.67×10^{-5} Pa) or better while the sputtering was carried out in Ar plasma with a pressure of 5 mTorr (0.67 Pa). The distance between the targets and substrate was approximately 13 cm and the deposition was performed at room temperature, although there was a nominal rise in temperature when multiple samples were sputtered consecutively.

3.1.2 Deposition of Cr

Prior to depositing the Cr onto the wafers, a 20-30 s hydrofluoric (HF) dip of concentration 10:1 was used to remove a native oxide layer so as to allow good electrical contact between the Cr electrodes and the $Si_{1-x}Ge_x$ alloy. The Cr was sputtered using the same RF sputtering system. The deposition parameters were identical to that of the Si and $Si_{1-x}Ge_x$ with an RF power of 200 W applied to the Cr target, a gas flow of 25 sccm, and a substrate bias of 150 V. As before, background pressure was kept at or below 6.5×10^{-4} while sputtering was carried out in Ar with a pressure of 5 mTorr. With an estimated deposition rate of 2.5 nm/min and a sputtering time of 1 h, the Cr thin film is approximated at 150 nm.

3.1.3 Annealing and Crystallization

Post-deposition annealing was carried out to thermally induce crystallization of the as-deposited thin films and was performed in a low pressure chemical vapor deposition (LPCVD) tube furnace with process and backfill gas flow of N_2. The profile of the anneal is shown in Fig. 3-1. The pressure was kept at 300 Torr with backfill flow at 100-150 sccm while the process flow was allowed to fluctuate to ensure constant pressure. The annealing temperature (T_{anneal}) was carried out at two different temperatures of 600 °C and 700 °C and the anneal time (t_{anneal}) for each temperature was 1 h.

The samples were loaded with several dummy wafers in between each device wafer and then slowly loaded into the furnace as to not thermally shock the wafers and allow uniform thermal expansion of the $Si_{1-x}Ge_x$ thin film. During the anneal, the

temperature was carefully ramped to the annealing temperature, T_{anneal}, and once that temperature was reached the wafers remained in the furnace for the predetermined anneal time, t_{anneal}. After the anneal was completed the temperature was carefully ramped to a lower set point and the wafers were slowly removed from the furnace again to avoid thermal shock.

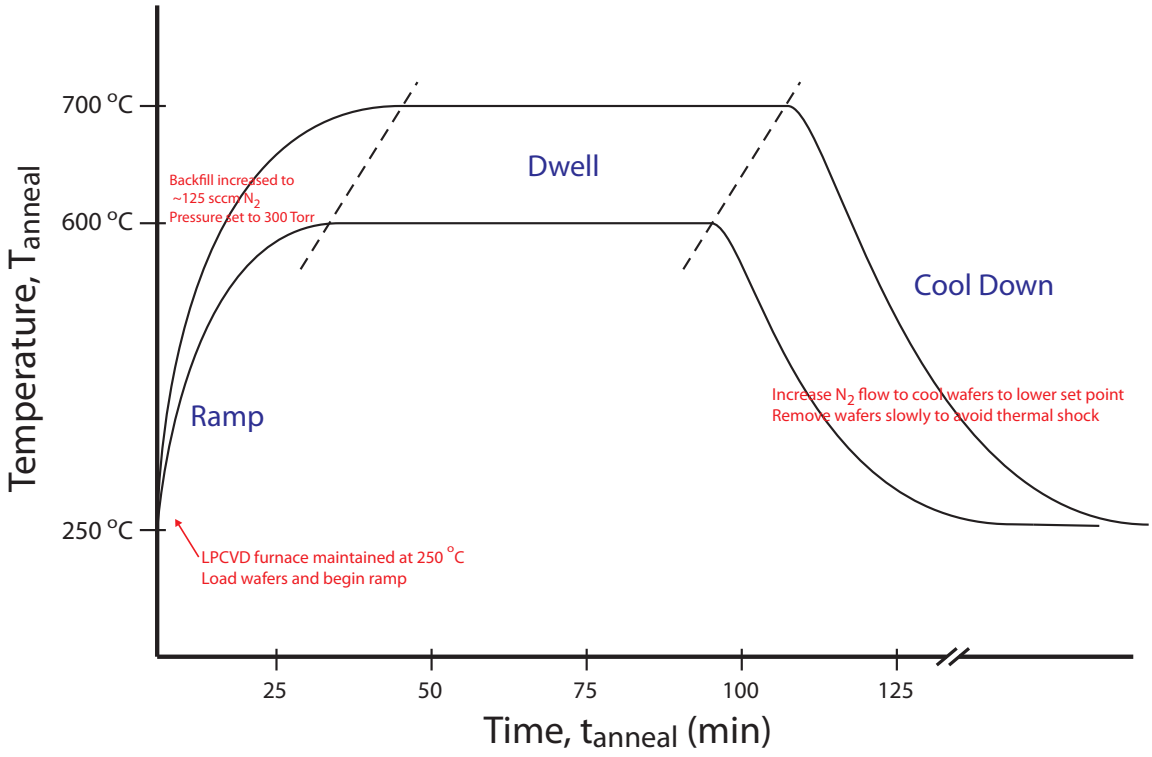

Figure 3-1 Anneal profile for wafers with $Si_{1-x}Ge_x$ thin film.

3.2 Testing and Characterization

Both the as-deposited and annealed $Si_{1-x}Ge_x$ alloys were studied using X-ray diffraction (XRD), Raman spectroscopy, ellipsometry, scanning electron microscopy (SEM), and energy-dispersive X-ray spectroscopy (EDX). The XRD experiments were performed using an X'Pert X-ray diffractometer with Cu-Kα radiation ($\lambda = 1.54056\,\dot{A}$).

The diffractometer was operated at an accelerating voltage of 45 kV and a current of 40 mA. All spectra were recorded using a grazing angle of 1° and 2θ between 20° and 65° with a scan step size of 0.05° and scan time of 1.0 s/step.

Reflectance measurements were taken for all samples at each anneal temperature. The measurements were taken using a Filmetrics F20-UV with a wavelength range of 200nm – 900nm.

The Raman measurements were carried out using a Renishaw Raman spectrometer. The samples were excited at room temperature using a 633 nm at 50x long with 100% power and an integration time of 40 s.

A Zeiss MERLIN scanning electron microscope was used for both imaging the samples and for acquiring the EDX spectra with an attached Bruker QUANTAX microanalysis system.

3.3 Electrode Patterning

3.3.1 Mask Design

The mask design for the electrode pattern was completed in AutoCAD and then exported to software that is compatible with a photomask laser writer. The design of the electrode array mask is shown in Fig. 3-2 and consists of several inter-digitated fingers. The spacing of L and w vary to keep the total resistance R as comparable to ensure accurate measurements and calculations of the resistivity. The values of L and w are shown in table 2 along with h and the number of fingers, n.

Since there are five values for *L* and *w* each cell consists of a set of five electrodes with a total of 29 cells per wafer. The spacing between the end of one finger and the base of the fingers, labeled *x*, is designed to be much greater than *L* since the electric field at the corner can be difficult to account. The inter-digitated fingers' leads connect to pads large enough to accommodate electrical test probes and reach far enough apart so that there is no interference between them.

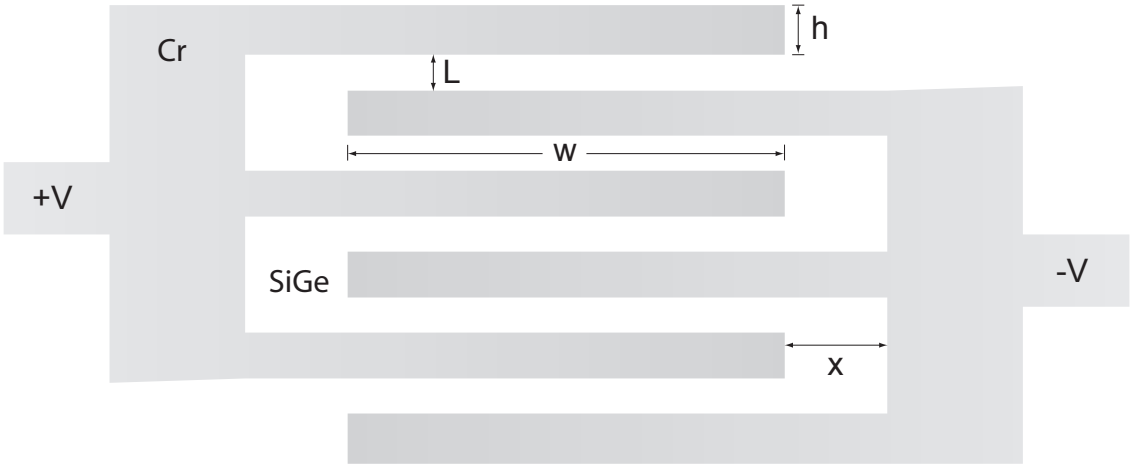

Figure 3-2 Mask design with various spacing parameters.

Table 2 Spacing parameter values for the inter-digitated finger electrodes.

L (μm)	w (mm)	h (μm)	n
2.5	2.5	10.0	10
5.0	5.0	10.0	10
10.0	10.0	10.0	10
20.0	10.0	20.0	20
30.0	10.0	20.0	30

3.3.2 Photolithography

Device wafer fabrication was performed in a photolithography hood with a negative mask and a negative resist. The negative resist that was selected was Futurrex CP 3000Y. A final spin speed of 5000 RPM for 40 s was chosen to achieve a resist layer thickness between 2100 – 2300 nm. Prior to spinning on the resist, the wafer was cleaned using acetone, methanol, and isopropanol alcohol (IPA), respectively.

The spin parameters for the resist deposition is start with a ramp at 500 RPM for 5 s and then gradually increase up to 5000 RPM. Once up to the set spin speed, spinning continued for 40 sec. A liquid primer was first applied on the wafer to ensure good adhesion of the resist. The primer was allowed to sit for one minute and then spun off. After doing so, the PR was applied by hand while being cautious to not drip or allow bubbles to form on the surface. Since this particular resist has a very high viscosity at room temperature, micro bubbles can easily form and the resist must be handled carefully.

After the resist was spun on, the wafer was placed on a hotplate for a pre-exposure or soft bake at 150 °C for one minute. After the soft bake and allowing to cool briefly the wafer was placed in a Karl Suss contact aligner for exposure with the appropriate mask. Each wafer was exposed using 365 nm light for 10 s. The contact aligner had an average intensity of 10 mW/cm^2 and with an exposure time of 10 s gives a dose of 100 mJ/cm^2.

After exposure, the wafer was once again placed on a hotplate for a post-exposure bake (PEB) at 100 °C for one minute. Using RD-6 developer by Futurrex, the wafer was

developed with slight agitation for approximately 15 s. Immediately after developing the wafer was rinsed with DI water for several seconds and then dried using a N_2 air gun. Finally, the wafer was examined using an optical microscope to ensure the Cr electrodes have been patterned correctly and that there was no more resist remaining.

Subsequent to inspection, the Chromium electrodes were etched in a wet etch solution. Finally, the resist was stripped by placing it in an acetone bath for approximately 15 s. This process is described illustratively in Fig. 3-3.

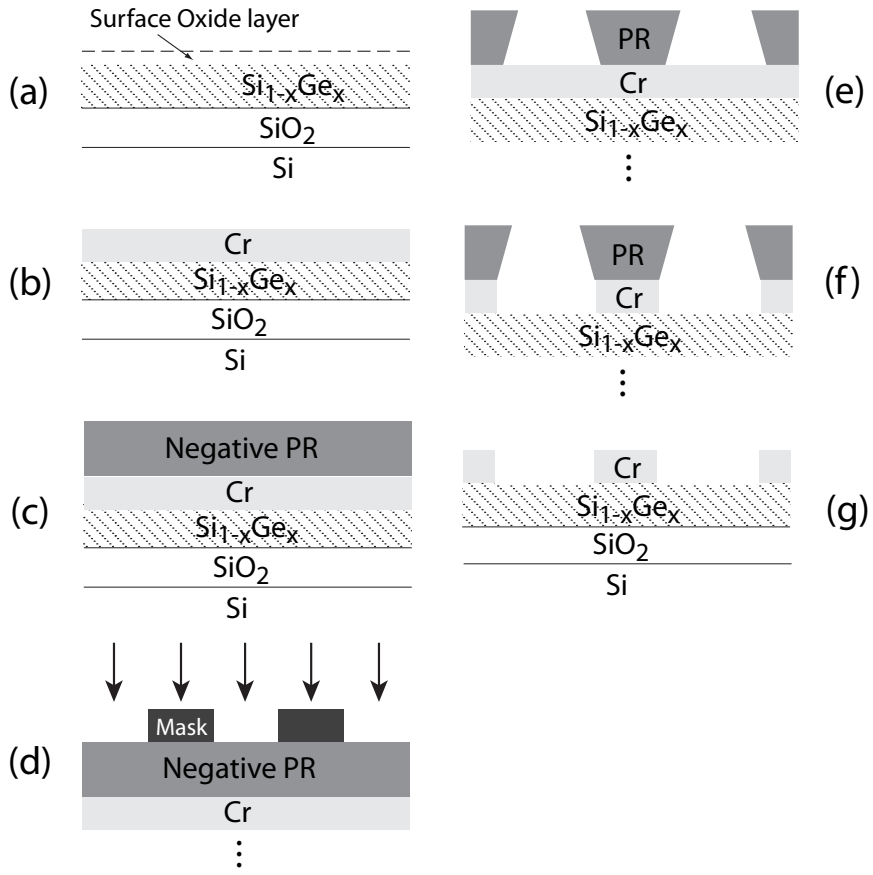

Figure 3-3 Photolithography process. (a) Sample is prepared by removing surface oxide layer so (b) deposited Cr makes good contact with SiGe layer. (c) Negative photoresist is spun on and then (d) exposed to 365 nm light. (e) Photoresist is developed and then (f) exposed Cr is etched leaving (g) patterned Cr electrodes.

4. Results and Discussion

This chapter presents the results obtained from the testing and characterization of the $Si_{1-x}Ge_x$ thin film alloy and provides a detailed discussion on the characteristics of $Si_{1-x}Ge_x$ and its photo and thermal response of a sensor device while comparing them to the optothermal behavior of similarly fabricated structures (sensors).

4.1 Compositional Analysis

The composition of the as-deposited thin films were determined by energy dispersive x-ray spectroscopy (EDX) in the range of 0-4 KeV with a scanning electron microscope equipped with an EDX module. With the exception of the Si-only samples, the analysis ensures that the EDX signal comes only from the deposited films due to the electron energy not being sufficient enough to penetrate into the substrate utilizing the depth penetration formula

$$R = \frac{0.0276\, A\, E_0^{1.67}}{Z^{0.89}\rho}\ \mu\text{m} \tag{14}$$

where R is the depth penetration, A is the atomic weight (g/mol), E is the beam energy (KeV), Z is the atomic number, and ρ is the density (g/cm^2).

The results are organized in table 1. The plots and convolution are shown in Figs. 4-1 – 4-3. As can be seen in the plots, there are localized peaks at approximately 1.19 KeV and 1.74 KeV, which correspond to Ge L-series and Si K-series, respectively.

Table 3 Summary of silicon and germanium content of the $Si_{1-x}Ge_x$ films from EDX measurements.

Sample Composition	*Element*	*Series*	*Un. C (wt%)*	*Norm. C (wt%)*	*Atom. C (at%)*	*Error (σ) (wt%)*
Si	Oxygen	K	1.75	1.62	2.80	0.31
	Silicon	K	106.22	98.38	97.20	5.80
	Totals:		**107.97**	**100.00**	**100.00**	
$Si_{1-x}Ge_x$	Silicon	K	76.22	70.55	86.10	4.17
	Germanium	L	31.81	29.45	13.90	1.78
	Totals:		**108.03**	**100.00**	**100.00**	
$Si_{1-x}Ge_x$	Silicon	K	53.25	48.92	71.23	2.93
	Germanium	L	55.60	51.08	28.77	3.09
	Totals:		**108.85**	**100.00**	**100.00**	

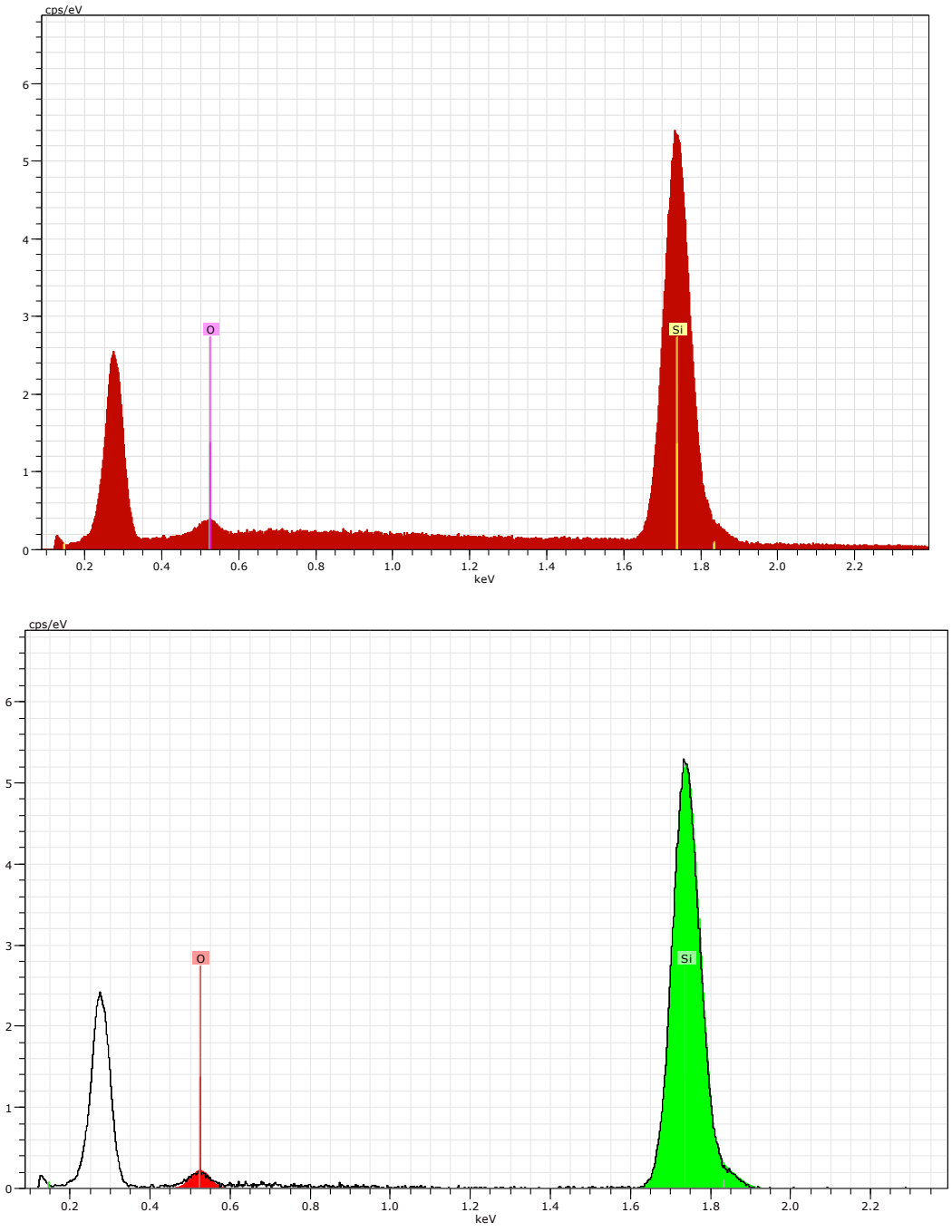

Figure 4-1 EDX measurements for Si. The horizontal axis is in the range 0 to 4 KeV and the vertical axis represents the number of relative counts.

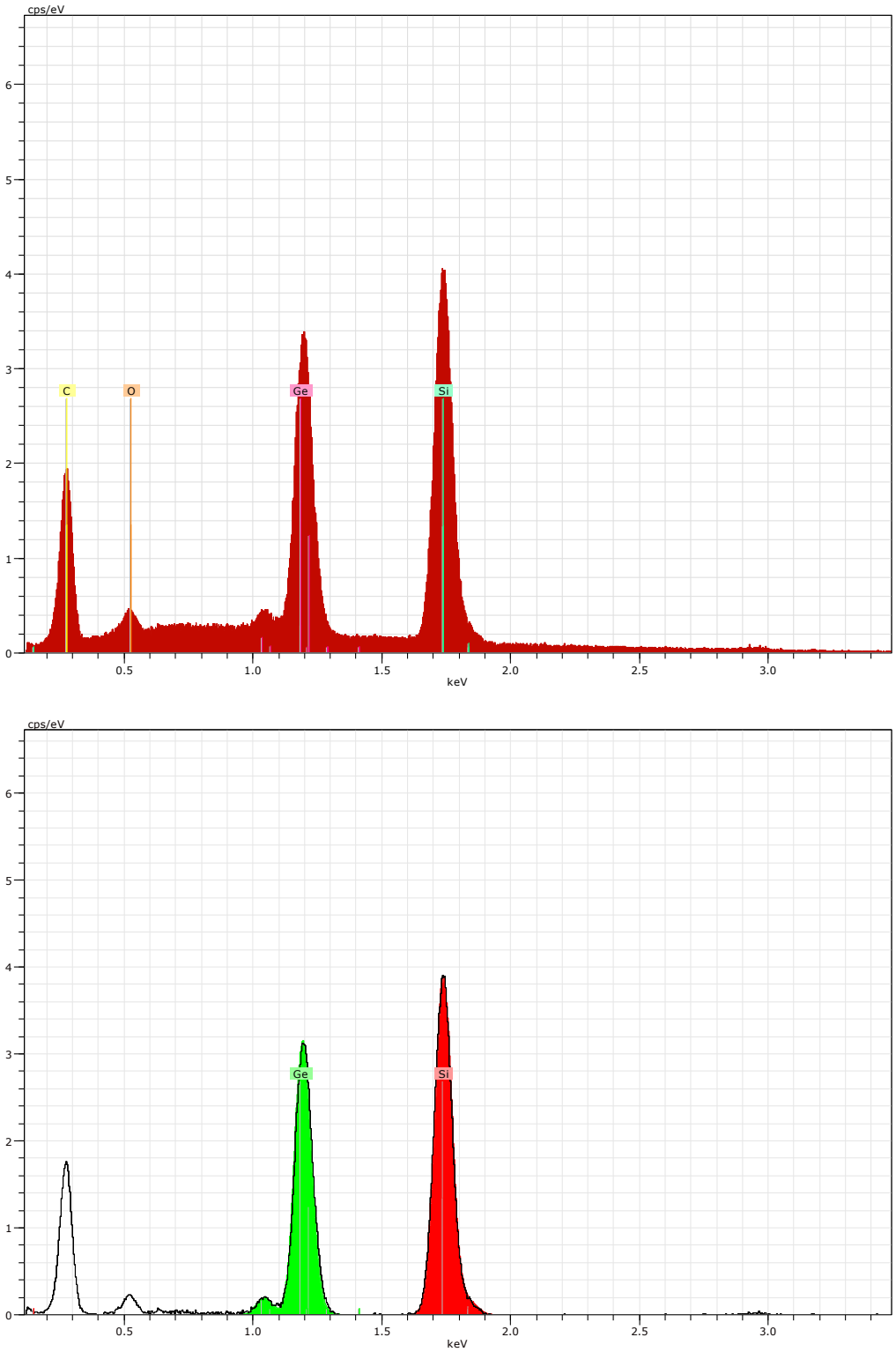

Figure 4-2 EDX measurements of $Si_{.85}Ge_{.15}$. The horizontal axis is in the range 0 to 4 KeV and the vertical axis represents the number of relative counts.

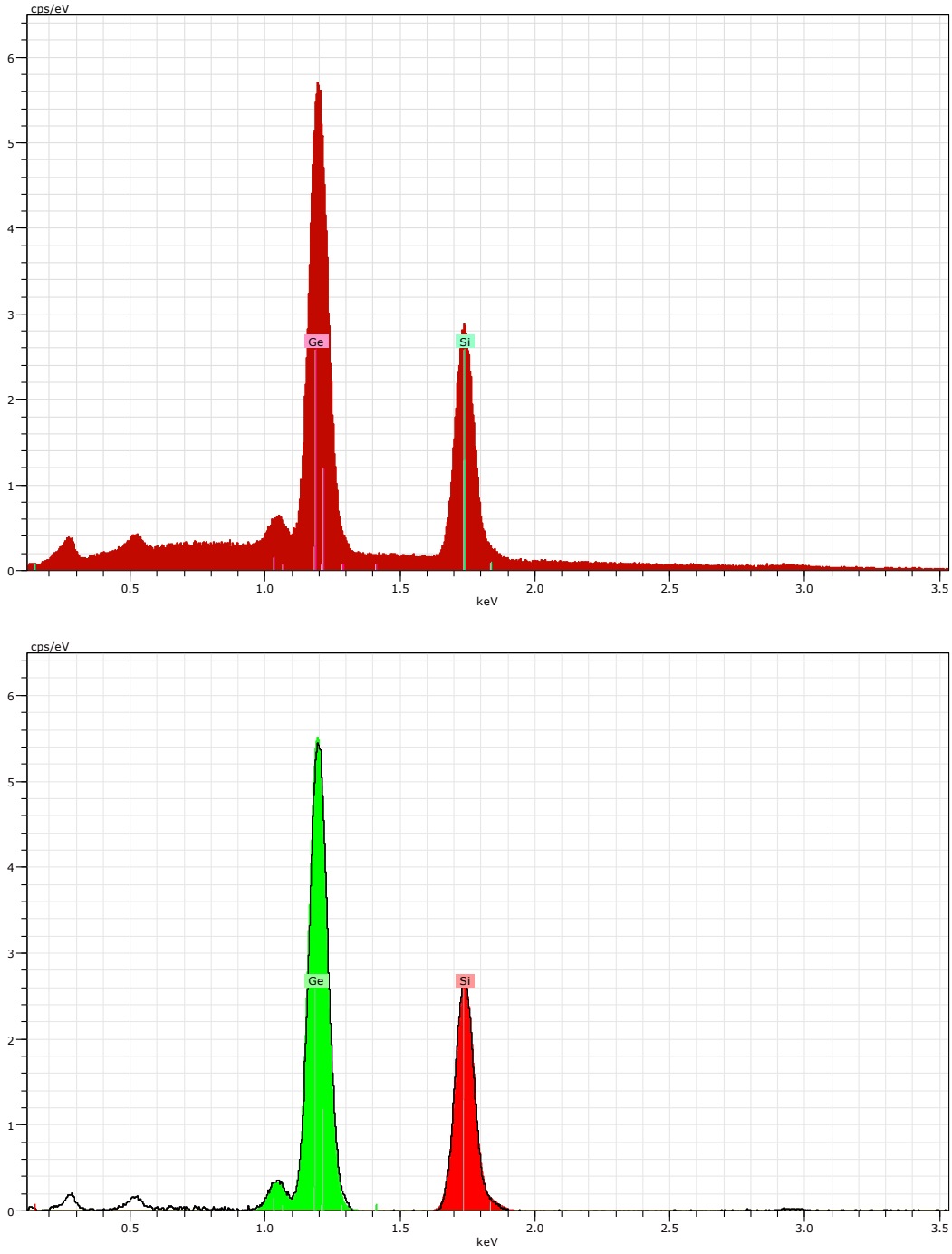

Figure 4-3 EDX measurements for $Si_{.70}Ge_{.30}$. The horizontal axis is in the range 0 to 4 KeV and the vertical axis represents the number of relative counts.

4.2 Annealing and Crystallization Comparison

The crystal grain nucleation in a-Si has been experimentally investigated since the end of the 1970s. The first studies were devoted to determination of the time evolution of the crystallized volume fraction by means of electrical conductivity or optical reflectivity measurements[39,40,41]. These studies showed that the crystalline fraction exponentially increases with time. The characteristic crystallization time, defined as the time needed to crystallize 67% of the a-Si layer (starting from the instant at which nucleation takes place), exhibits Arrhenius behavior. However, both electrical conductivity and optical reflectivity are sensitive only to the crystallized volume fraction and, as a consequence, such measurements do not give independent information on the density and the size distribution of the grains.

The crystalline structure for samples annealed at 600 °C is shown in Fig 4-4 through Fig. 4-6. As can be seen from the images in Fig. 4-4, there is no structure or signs of crystallization, which is expected knowing Si requires higher anneal time and/or temperature and agrees with XRD data. For $Si_{.85}Ge_{.15}$ the polycrystalline structure is apparent (see Fig. 4-5) with a grain size of approximately 2-4 μm. As with the low germanium content sample, $Si_{.70}Ge_{.30}$ has a polycrystalline structure (see Fig. 4-6) but with a grain size between 1 and 2 μm. Samples annealed at 700 °C are shown in Fig 4-7. The most noticeable difference is the observable structure in the pure Si sample.

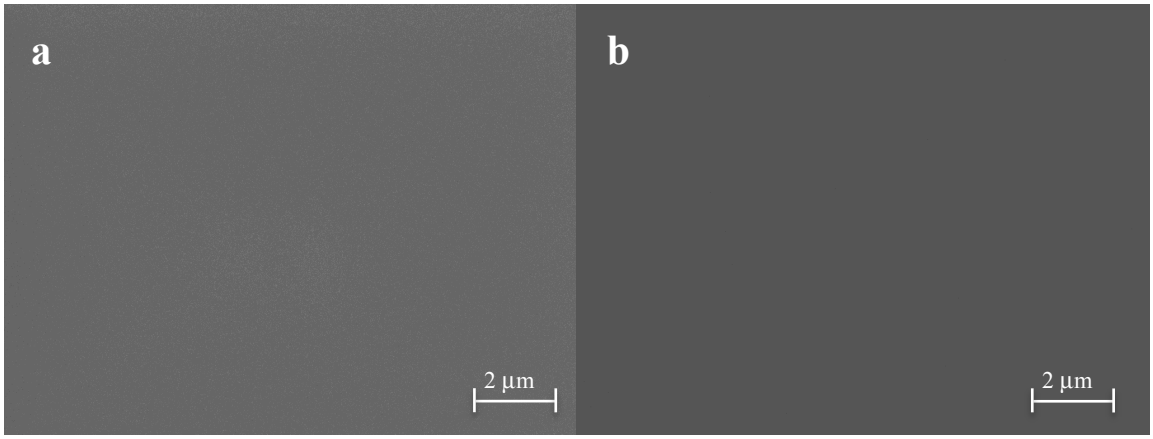

Figure 4-4 SEM images showing structure of thin film for Si at 600 °C for 1 hr. shown at (a) 20K magnification with (b) as deposited film used as reference.

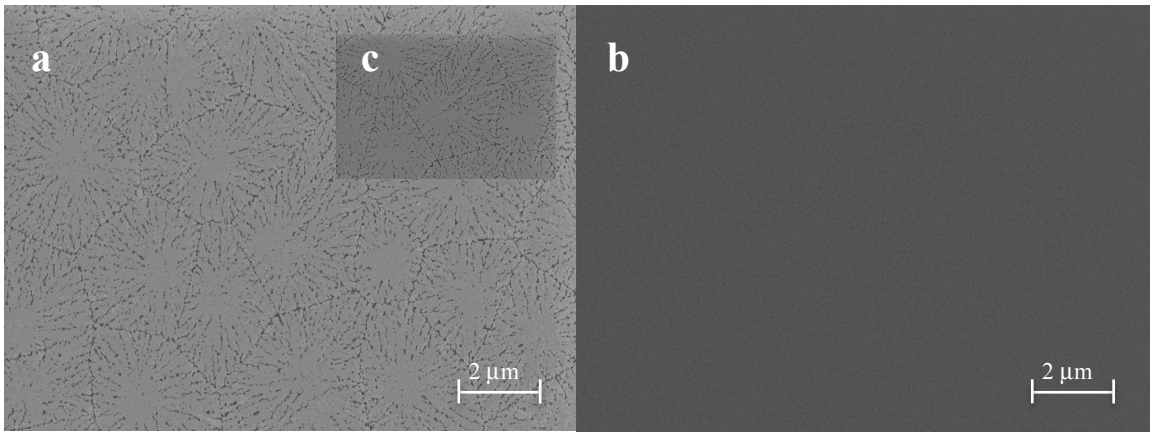

Figure 4-5 SEM Images showing structure of thin film for $Si_{.85}Ge_{.15}$ annealed at 600 °C for 1 hr. shown at (a) 20K magnification with (b) as-deposited film used as reference and insert (c) showing structure at 40K magnification.

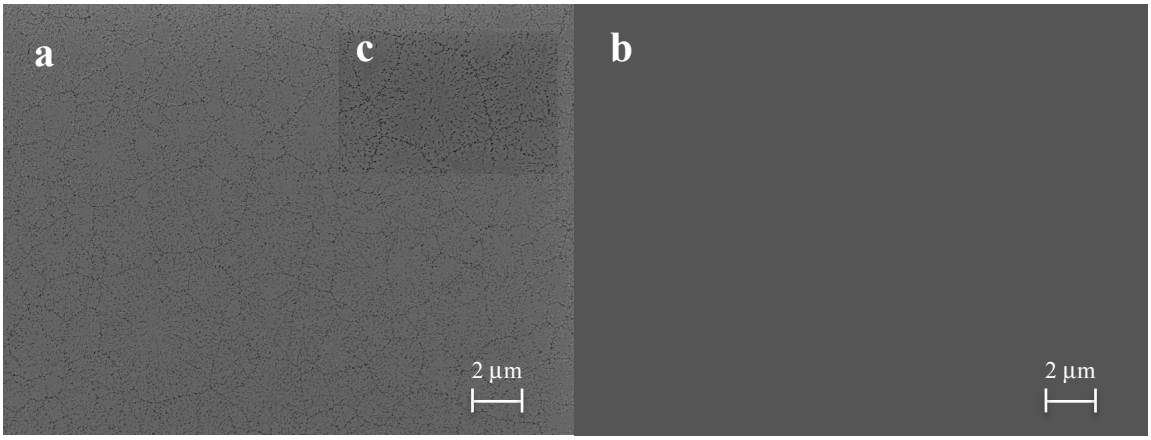

Figure 4-6 SEM images showing structure of thin film for $Si_{.70}Ge_{.30}$ annealed at 600 °C for 1 hr. shown at (a) 10K magnification with (b) as-deposited film used as reference and insert (c) showing structure at 40K magnification.

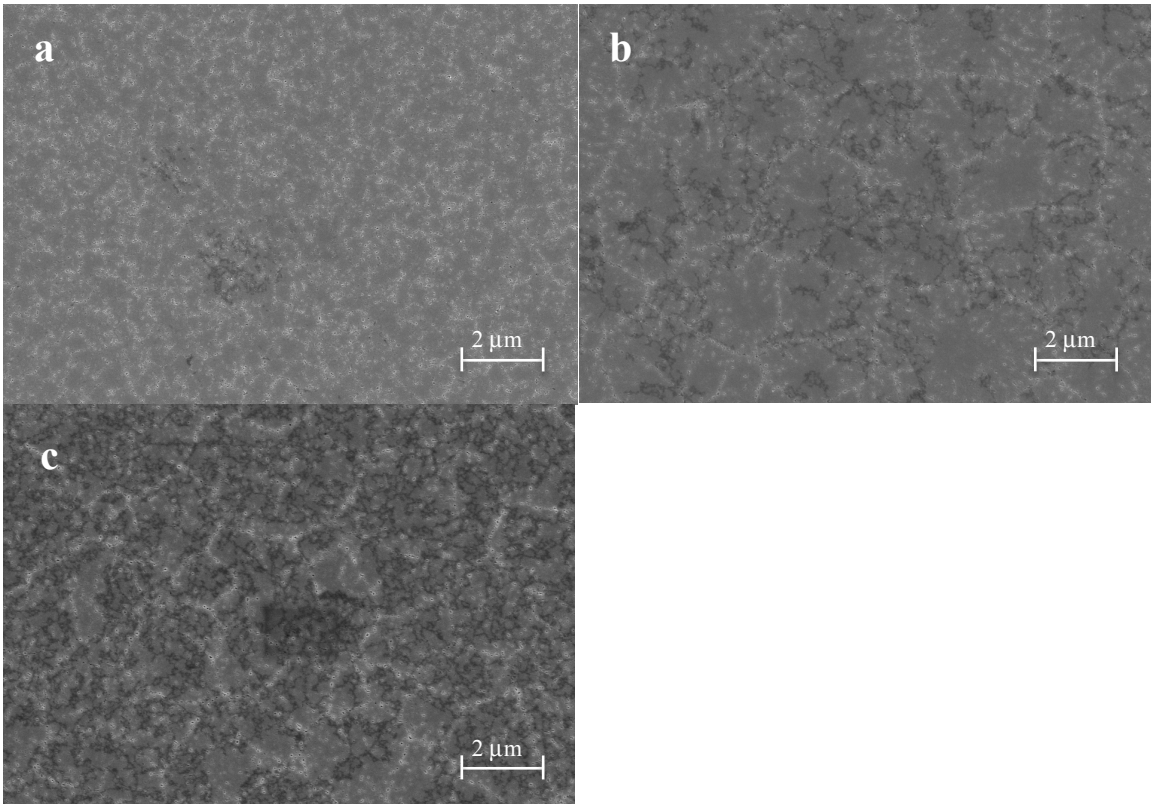

Figure 4-7 Structure of thin films for (a) Si, (b) $Si_{.85}Ge_{.15}$, and (c) $Si_{.70}Ge_{.30}$. All films were annealed at 700 °C for 1 hr. and shown at 20K magnification

4.2.1 Reflectrometry

In Fig. 4-8, the reflectance measurements are shown for various films at various anneal times with a close look at the UV region in Fig. 4-9. As the amorphous-to-crystalline transition occurs the spectra appears to left shift and displays an increases in reflections. The samples that contain Ge crystallize near 600 °C while, although the reflectance changes, the Si sample requires a higher temperature.

To compare the crystallinity of the compositionally varying films between as-deposited and annealed samples, the reflectance spectra data of a single crystalline silicon and sputter deposited amorphous silicon sample are presented[42] (see Fig. 4-10). At 275 nm and 375 nm wavelengths silicon shows the characteristic reflectance peaks. Thus, indirectly the degree of crystallinity of poly-Si can be compared by comparing the reflectance peak intensity.

It can also be seen that the pure Si sample annealed at 600 °C is very comparable to that of a-Si. This indicates that there is little to no structure formation and that a higher anneal time and/or temperature are required to induce crystallization whereas the samples containing Ge show characteristic peaks.

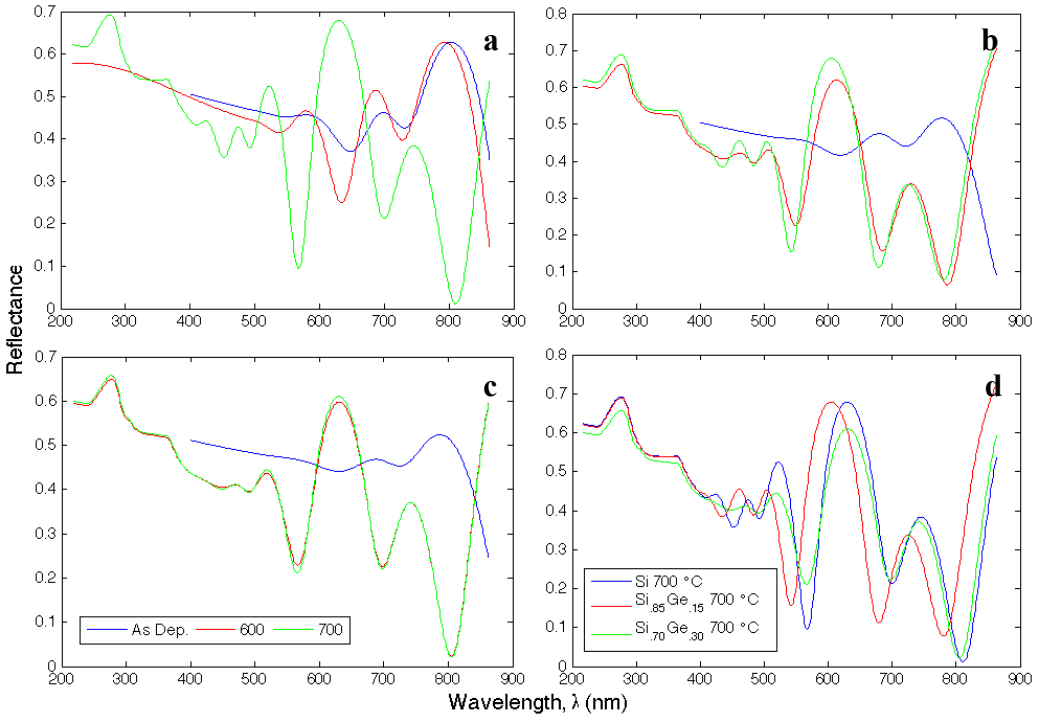

Figure 4-8 Reflectance measurements of a) Si on SiO_2, b) $Si_{.85}Ge_{.15}$ on SiO_2, c) $Si_{.70}Ge_{.30}$ on SiO_2, and d) a comparison of varying compositional alloys annealed at 700 °C.

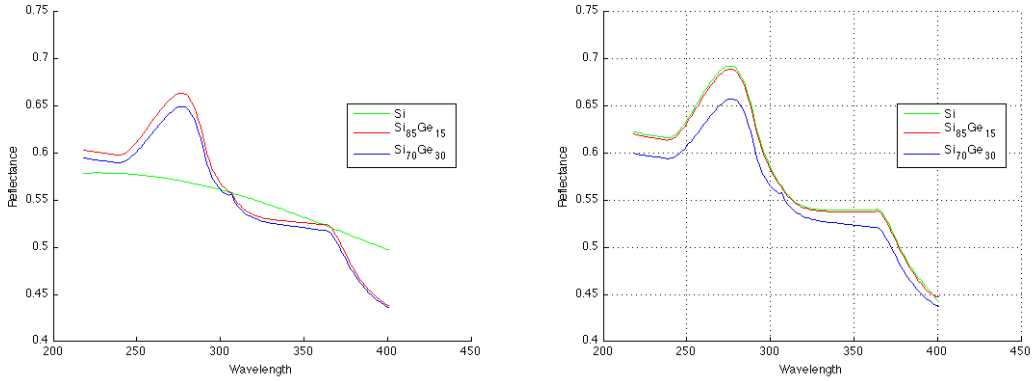

Figure 4-9 A comparison of reflectance in the UV region for $Si_{1-x}Ge_x$ films annealed at 600 °C (left) and 700 °C (right).

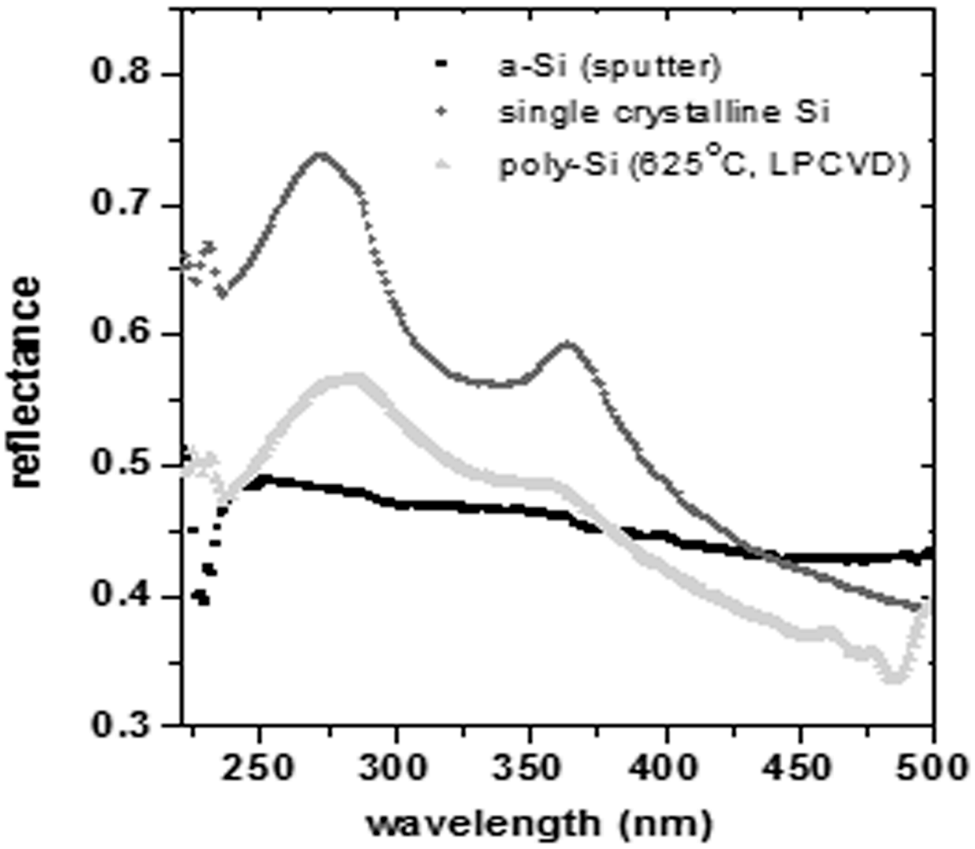

Figure 4-10 Reflectance of deposited LPCVD poly-Si compared to reflectance data of sputter deposited amorphous silicon and single crystalline silicon[42].

4.2.2 X-Ray Diffraction

From the XRD spectra shown in Figs. 4-11 it can be seen that the annealed Si wafer has not crystallized at anneal temperature of 600 °C and is still amorphous, which is expected since it requires a higher anneal temperature and/or longer anneal time. However, its reflectance measurements (see Fig. 4-8), show a change implying that there is some change in the microstructure of the Si thin film with short range order. Reaching

an anneal temperature of 700 °C the Si film shows diffraction peaks at the expected values.

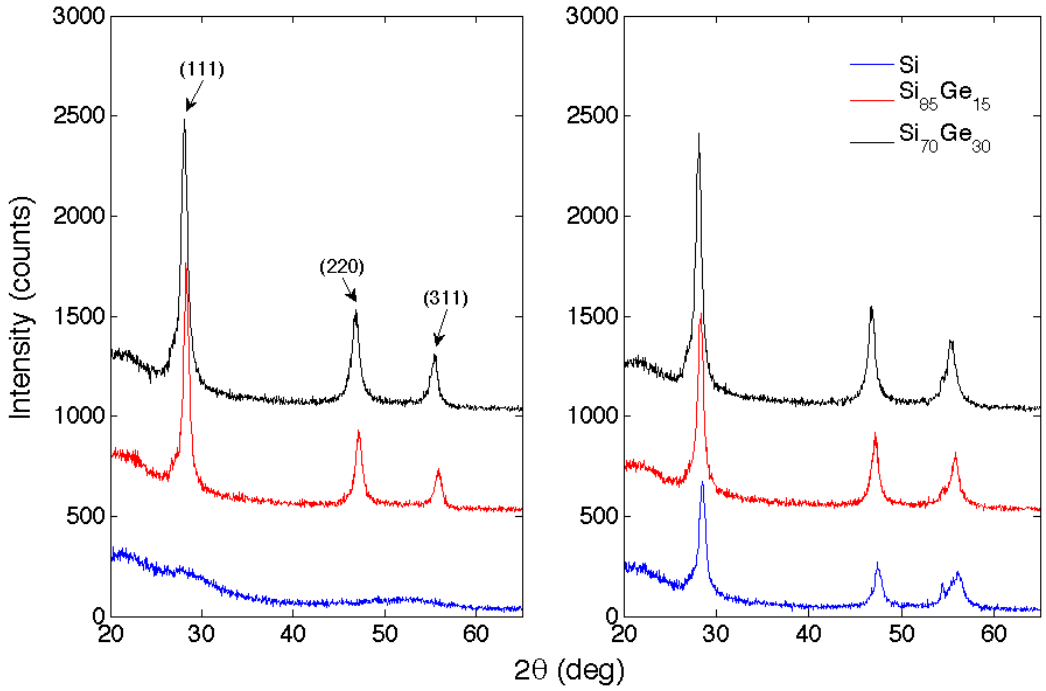

Figure 4-11 XRD spectra for various $Si_{1-x}Ge_x$ films annealed at 600 °C (left) and 700 °C (right) for 1 h. All samples that were not annealed (as-deposited) are comparable to that of Si and are treated as the same. The curves have been vertically displaced for clarity.

For the set of wafers with germanium in them that were annealed at 600 °C, the (111) dominant peak was observed at 28.28° for $Si_{.85}Ge_{.15}$ and 28.13° for $Si_{.70}Ge_{.30}$, which corresponds very closely to Si powder reported value of 28.443°. The other peaks correspond to (220) and (311) and are 47.18° and 55.93°, respectively, for $Si_{.85}Ge_{.15}$ and 46.83° and 55.38°, respectively, for $Si_{.70}Ge_{.30}$. Also, the absence of dual peaks at these positions confirm that the thin film is indeed $Si_{1-x}Ge_x$ rather than Si and Ge clusters.

As for the wafers that were annealed at 700 °C, the (111) dominant peak was observed at 28.48° for Si, 28.33° for $Si_{.85}Ge_{.15}$, and 28.13° for $Si_{.70}Ge_{.30}$. This data, along

with the remaining peaks, all of which are listed with their peak intensities, are summarized in Table 4. It is interesting to note that the intensity of the three diffraction peaks increased with Ge content but the peak intensity varied with annealing temperature showing a decrease at the (111) peak, an increase at the (311) peak, and both an increase and decrease at the (220) peak.

Compared to results reported in the literature, the progress of crystallization of the $Si_{1-x}Ge_x$ alloy films in this work was relatively quick. It has been reported that RF sputtered $Si_{1-x}Ge_x$ alloy films with germanium content < 0.49 were completely crystallized after furnace annealing at 550 °C for 24 h[43] with some reports requiring annealing at 700 C for 24 h[44] where as in this work the films begin to fully crystallize after 1 h at 600 °C. Overall, the measurements show a slight left-shift in 2θ arising from a change in the lattice constant. In this case, significant crystallization was achieved when annealing at or above a temperature of 600 °C for at least one hour.

Both Si and Ge have a diamond cubic structure and are fully soluble in one another (see phase diagram, Fig. 2-3) so that it is expected that the $Si_{1-x}Ge_x$ alloy has the same structure with a lattice parameter intermediate between that of pure Si and pure Ge. It has been reported[45] that the lattice parameter of the $Si_{1-x}Ge_x$ alloy at room temperature varies linearly from 0.54310 nm to 0.56575 nm as the Ge content increases from $x = 0$ to $x = 1$ (see Fig. 4-13). Also, an approximated value may be obtained using Vegard's law – an empirical rule – to find a linear relationship between the lattice parameters of a solid solution alloy and the composition of such alloy. Vegard's law can be mathematically expressed as

$$a_{Si_{1-x}Ge_x} = X_{Si}a_{Si} + X_{Ge}a_{Ge} \quad (15)$$

Table 4 Summary of peak diffraction angle and intensity (counts) for various film compositions. The numbers in bold correspond to the values of the peak intensities where a peak is expected after crystallization.

	Si			**$Si_{.85}Ge_{.15}$**			**$Si_{.70}Ge_{.30}$**		
	(111)	(220)	(311)	(111)	(220)	(311)	(111)	(220)	(311)
As-Dep.	**-** ***217***	**-** ***92***	**-** ***69***	**-** ***264***	**-** ***110***	**-** ***78***	**-** ***304***	**-** ***130***	**-** ***107***
600 °C	**-** ***218***	**-** ***85***	**-** ***70***	*28.28°* *1266*	*47.18°* *419*	*55.93°* *240*	*28.13°* *1485*	*46.83°* *531*	*55.38°* *309*
700 °C	*28.48°* *673*	*47.43°* *272*	*56.13°* *224*	*28.33°* *1017*	*47.18°* *418*	*55.83°* *322*	*28.13°* *1415*	*46.83°* *548*	*55.28°* *381*

where a_{Si} and a_{Ge} are lattice constants of the pure components and X_{Si} and X_{Ge} are their atomic fractions in the alloy. Knowing the composition of the thin films from EDX measurements and with $a_{Si} = 5.4311$ Å and $a_{Ge} = 5.46579$ Å, the lattice parameter can be found using Vegard's law:

$$Si_{.85}Ge_{.15} = (.861)(.54311) + (.139)(.56579) \text{ nm}$$

$$a = 5.4626 \text{ Å}$$

and

$$Si_{.70}Ge_{.30} = (.7123)(5.4311) + (.2877)(5.6579) \text{ Å}$$

$$a = 5.4964 \text{ Å}$$

There is also a relation between the lattice parameter and Bragg angle, θ, and is given by

$$a = \frac{\lambda\sqrt{h^2+k^2+l^2}}{2\sin\theta} \quad (16)$$

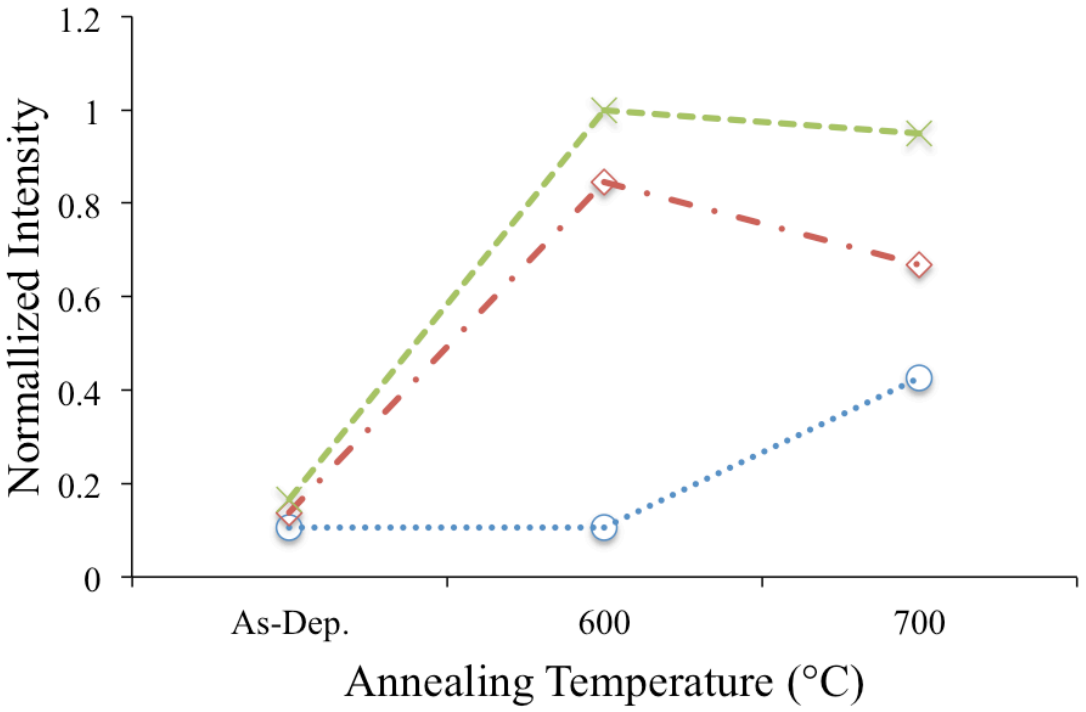

Figure 4-12 Relationship between normalized XRD (111) peak intensities and the annealing temperature. Green crosses represent $Si_{.70}Ge_{.30}$, red diamonds represent $Si_{.85}Ge_{.15}$, and blue circles represent Si

Using this relation and measured diffraction angles, a first-order estimate of the lattice parameter can be calculation. For $Si_{.85}Ge_{.15}$ the calculation gives $a = 5.4657$ Å and $Si_{.70}Ge_{.30}$ gives $a = 5.4943$ Å, which are close to the values obtained from Vegard's law with differences of $.0031$ Å and $.0021$ Å.

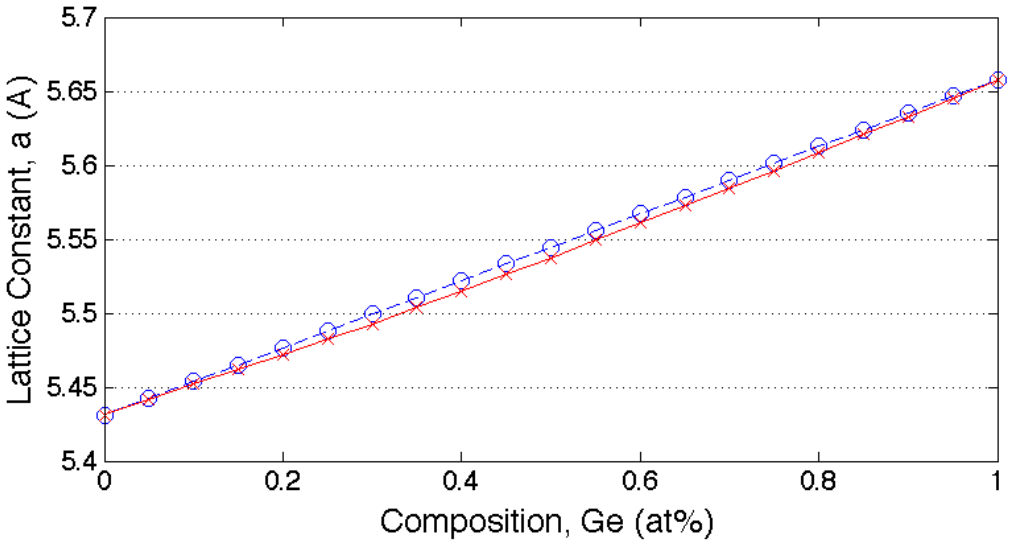

Figure 4-13 Lattice parameter of the $Si_{1-x}Ge_x$ system as a function of Ge composition[45]. Red crosses indicate experimentally measured lattice parameters and blue circles indicate lattice parameters calculated using Vegard's law.

4.2.3 Raman Spectroscopy

The XRD observations were supported by Raman studies. Fig. 4-14 shows Raman spectra of the $Si_{1-x}Ge_x$ films that were prepared by RF sputtering. The Raman data has been normalized so that for each spectrum the highest peak corresponds to 1000 counts as well as each spectrum being shifted vertically by 1000 counts for clarity. The films that were annealed shows a crystalline structure by observation of the three peaks of Ge-Ge, Si-Ge, and Si-Si in the Raman spectra while the as-deposited films show no peaks and implies an amorphous structure. The degree of crystallinity of the films depends on the annealing temperature (and time).

The as-deposited spectra (black) corresponds to the respective wafer. First off, there is a definite change in crystallinity as can be seen by the increase Si-Si mode peak (~530 cm^{-1}) intensity compared to the as-deposited films. The three optical-phonon

modes associated with Ge-Ge, Si-Ge, and Si-Si vibrations are seen near 300, 400, and 530 cm^{-1}, respectively, in the $Si_{70}Ge_{30}$ composition, although they aren't in $Si_{85}Ge_{15}$ and the pure Si wafer.

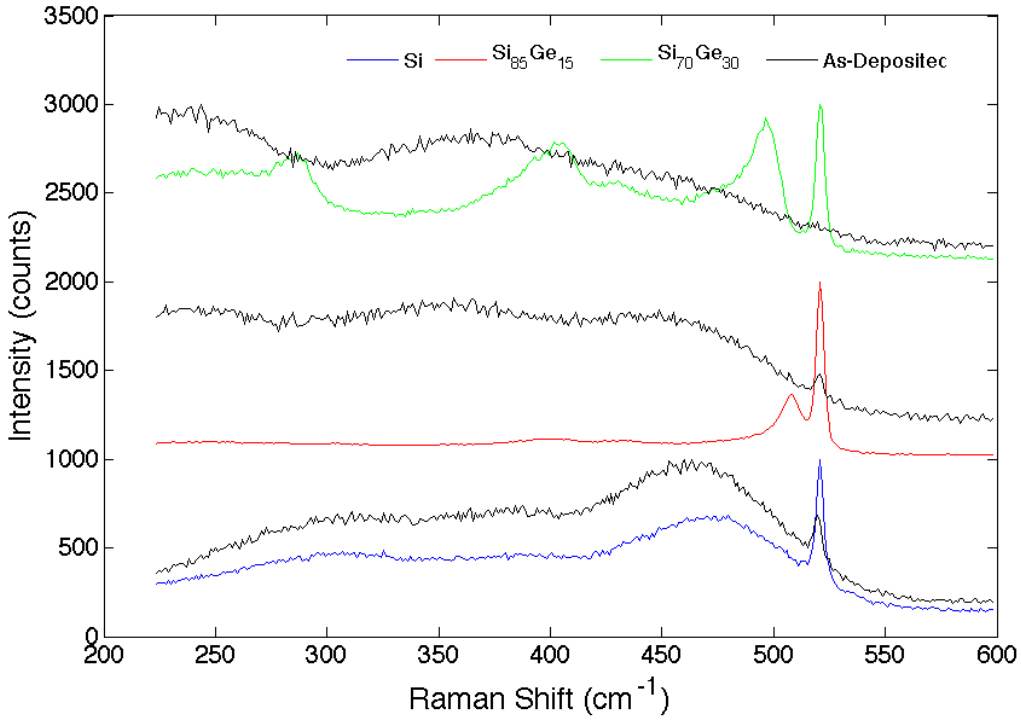

Figure 4-14 Raman spectra of as-deposited and annealed $Si_{1-x}Ge_x$ films prepared by RF sputtering at room temperature. Each Raman spectrum is shifted by 1000 counts for illustration purposes.

4.3 Electrical Testing

In this section the results and analysis of the measurements on the electrical properties of amorphous and poly Si and $Si_{1-x}Ge_x$ are presented. The aim is to present data on the properties themselves and to indicate how the properties are related to both thermal history and compositional dependence. The samples used in this study were comprised of the same Si and $Si_{1-x}Ge_x$ thin films deposited on Si substrates with a 500 nm SiO_2 layer. Samples were annealed at 600 °C, 700 °C for all compositions and were

compared against as-deposited samples. The resistivity, and hence the conductivity taking $\sigma = 1/\rho$, of the $Si_{1-x}Ge_x$ thin film alloys were characterized using a Keithly Series 2400 Source Meter with a custom semiconductor characterization system and measured by simply using a 2-point probe sweep to obtain an I-V curve. Photoconductivity was measured using the same procedure but with the samples under illumination in a dark environment. All samples were kept a room temperature.

4.3.1 Variations in Concentration

According to the compositional analysis, the $Si_{1-x}Ge_x$ samples have compositions of 86.1% and 13.9% by atomic weight and 71.23% and 28.77% by atomic weight with one sample consisting of only Si. It is shown in Fig. 4-15 the conductivity dependence on the amount of Ge in a sample. It is not surprising that the most conductive samples are those with higher content of with the exception of a pure Si sample annealed at 700 °C.

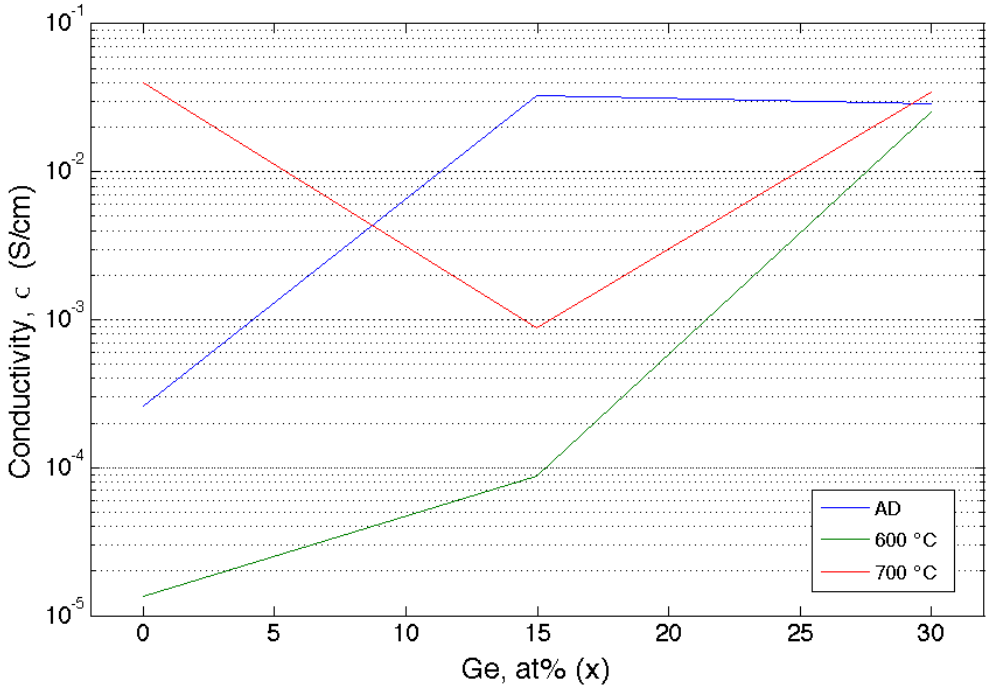

Figure 4-15 Conductivity, σ, for $Si_{1-x}Ge_x$ films at different Ge concentrations (x) held at room temperature.

4.3.2 Variations in Temperature

In Fig. 4-16 the dependence of the photoconductivity on annealing temperature is shown and a general trend can be seen with high conductivity with the as-deposited and 700 °C annealed samples with a lower conductivity at an anneal temperature of 600 °C.

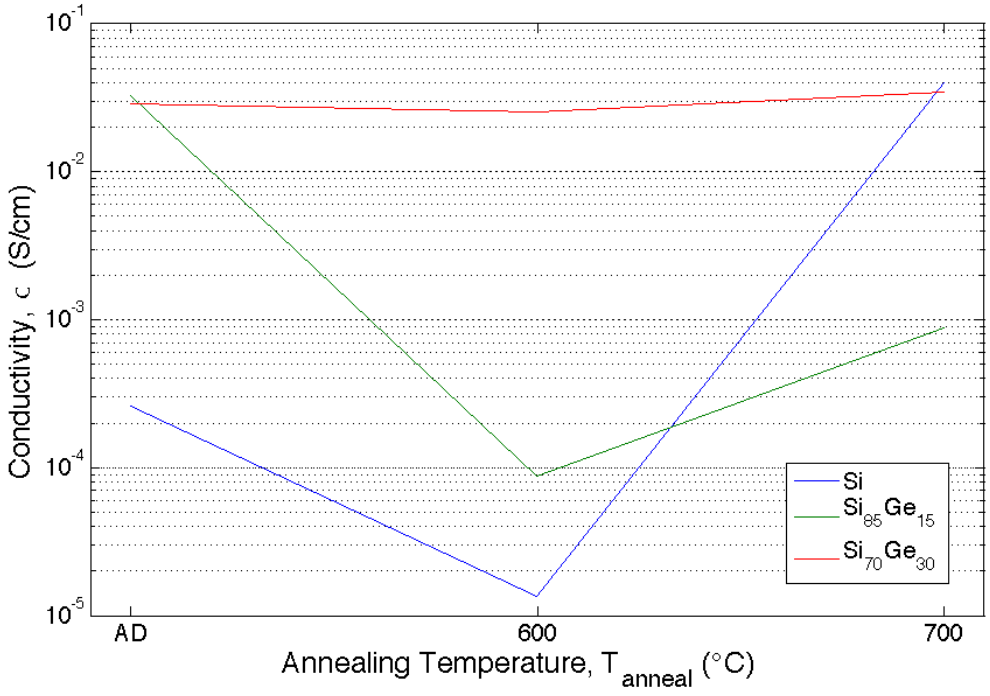

Figure 4-16 Photoconductivity dependence on annealing temperature for various compositions of $Si_{1-x}Ge_x$ alloy. Measurements were taken at room temperature

4.3.3 Variations in Spacing

The results for change in resistivity for electrode spacing is shown in Fig. 4-17 through Fig. 4-19. As expected, there is little change in the resistivity since this is an intrinsic property and the data suggest this. However, there should be a noticeable change in the photoconductivity as increasing the spacing between the electrodes increases the active area in which photoconductivity can occur. The is a limiting factor to increasing the distance too much though as an increase in available carriers with distance will be dominated by a decreasing electric field.

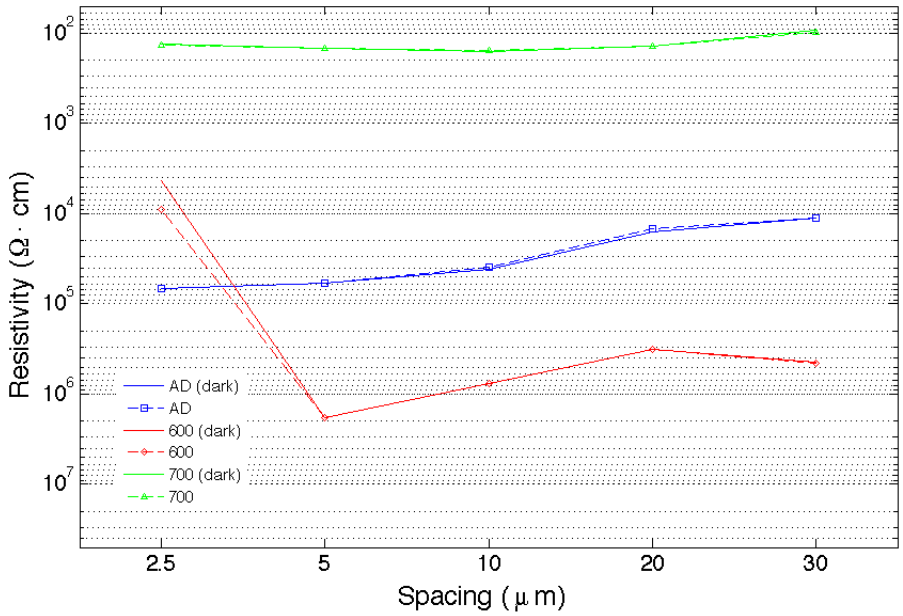

Figure 4-17 Si on Si/SiO_2 wafers with electrode spacing between 2.5 μm and 30 μm

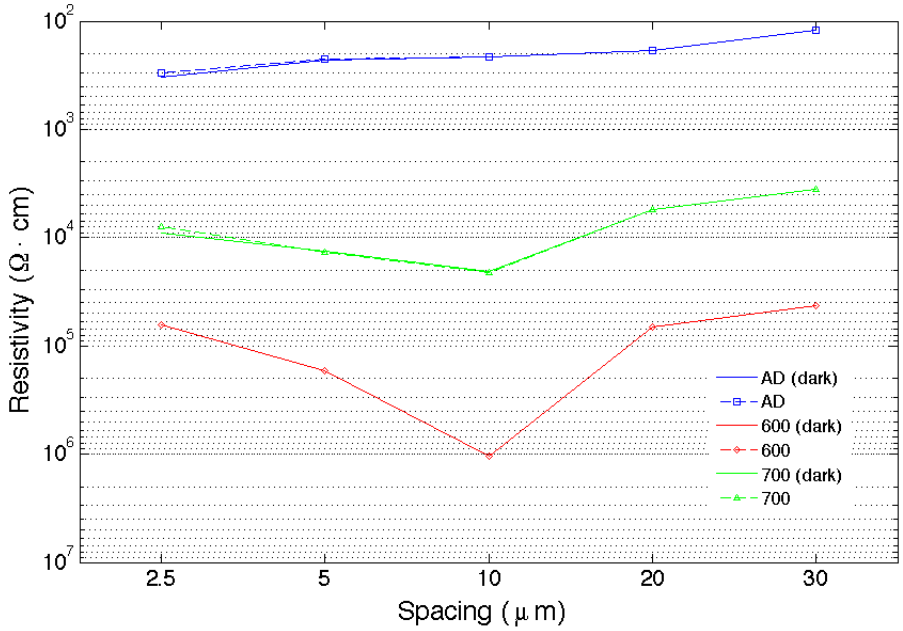

Figure 4-18 $Si_{.85}Ge_{.15}$ on Si/SiO_2 wafers with electrode spacing between 2.5 μm and 30 μm

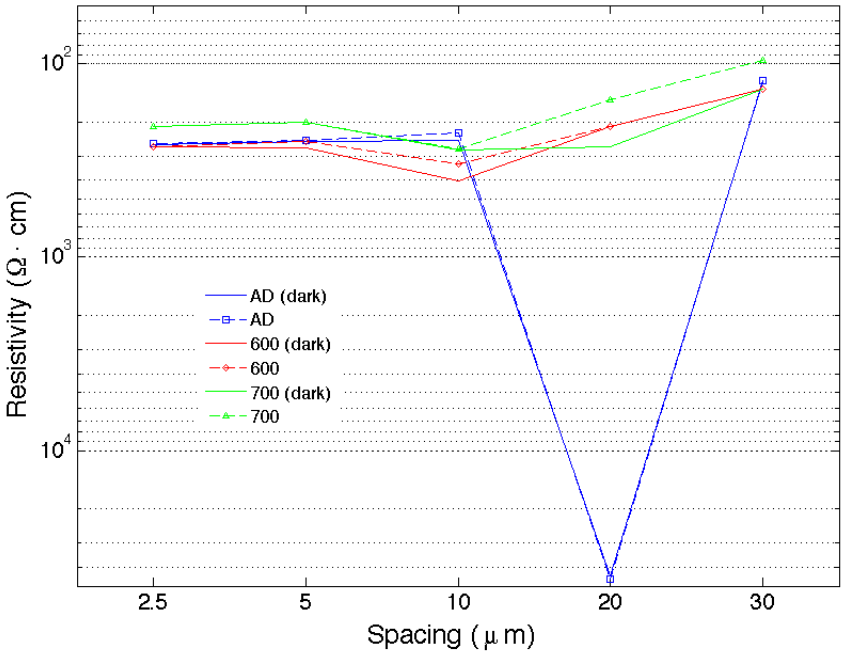

Figure 4-19 $Si_{.70}Ge_{.30}$ wafers with electrode spacing between 2.5 μm and 30 μm

4.4 Discussion

Much research has been dedicated to study on operating temperature effects to the semiconductor with its relation to conductivity-temperature dependence[46,47] and it has been shown extensively that the dark conductivity, σ_D, of a series of $Si_{1-x}Ge_x$ alloy decreases with inverse temperature. Conversely, σ_D increases monotonically with an increase in Ge (by atomic percentage) [46]. However, some have shown that the conductivity dependence on temperature begins to vanish for higher Ge content, that is $x > 0.5$.

Knowing this about the dark conductivity, if we assume that all the photons are absorbed then the steady-state photoconductivity is given by

$$\sigma_{Ph} = \frac{q\eta I\lambda\tau(\mu_e + \mu_h)}{hcd}$$

where q is the absolute value of the electronic charge, η is the quantum efficiency for photo carrier generation, I is the intensity of the light illuminated on the surface, λ is the wavelength, μ is the photo carrier drift mobility, τ is its lifetime, and d the sample thickness. However, the transmitted intensity through the specimen with thickness d is actually $I_0 \exp(-\alpha d)$ and absorption is determined by the intensity lost in the material $I_0[1 - \exp(-\alpha d)]$, which defines photoconductivity as

$$\sigma_{ph} = \frac{q\eta I_0(1 - e^{-\alpha d})\lambda\tau(\mu_e + \mu_h)}{hcd}$$

A well established approach to improving the electronic and structural properties of both amorphous and polycrystalline Si (as well as SiGe alloys) is to incorporate hydrogen into the material[48,49,50] and, in many cases, results in the neutralization of electrically active defects, which is crucial for device applications. On the other hand, photoconductivity measurements[51] on high temperature and laser annealed samples provide an indication that H incorporation might also induce non-beneficial effects for device applications as at high temperatures the H is driven out the sample. If we take $\sigma_L = \sigma_{Ph} - \sigma_D$, where σ_L is defined as the conductivity due to light illumination, we can see the results in Fig. 4-20. These values of light enhancement have been tabularized and can be compared against one another as shown in Table 5

There are two general trends that increasing the Ge content increases the conductivity and that samples annealed at 600 °C decrease in conductivity relative to the as-deposited (AD) samples but improve after annealing at 700 °C. This graph conforms

nicely to what is expected from increasing the amount of Ge in that the alloy decreases the energy band gap (see Figs. 2-7 and 2-8) allowing more electrons to be

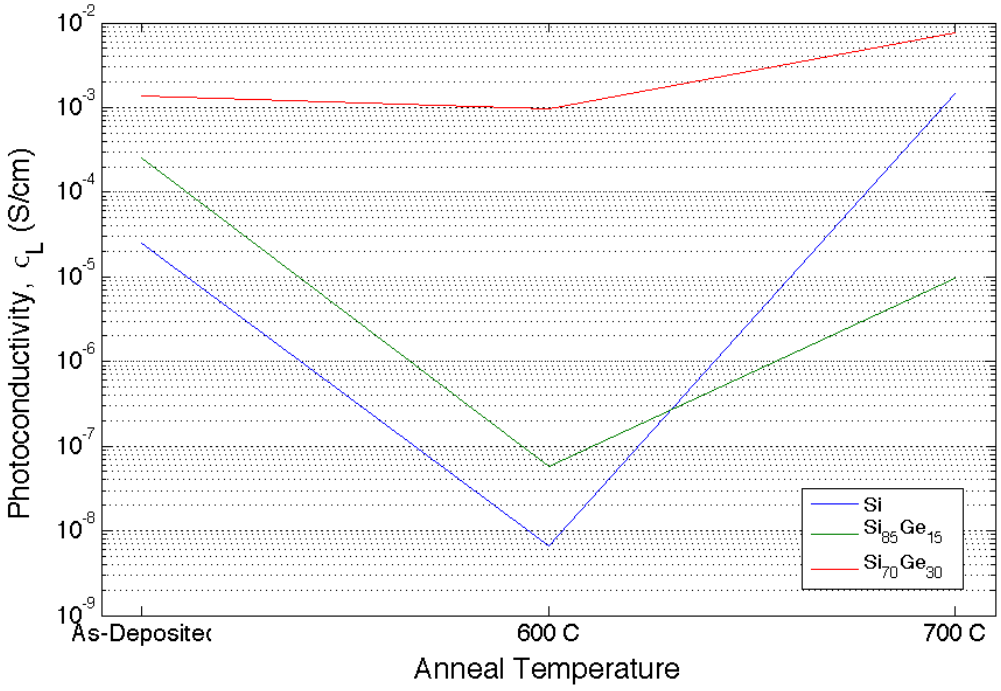

Figure 4-20 Conductivity due to light illumination, σ_L, of $Si_{1-x}Ge_x$ thin film alloy at various anneal temperatures

excited into the conduction band. However, the decrease in conductivity after annealing at 600 °C must be more carefully investigated as one would expect an increase, however slight, due to improvement in the ordering and arrangement of the polycrystalline structure, which can be confirmed by SEM analysis (see Figs. 4-4 to 4.6), and in the reflectance measurements (see Figs. 4-8 and 4-9) and XRD data (see Fig. 4-11).

However, there is a decrease in conductivity after annealing, which was not expected. It is proposed that this is attributed to the fact that although the band gap, E_g,

decreased, there is also a decrease in the available states in the conduction band, which can be explained by starting with the structural results obtained through XRD and Raman

Table 5 Light enhancement of as-deposited and annealed wafers. Values are represented as percentages in decimal form.

As-Deposited Samples					
	2.5 um	**5 um**	**10 um**	**20 um**	**30 um**
0 at% (Ge)	*0.02*	*0.13*	*6.05*	*7.80*	*1.56*
15 at%	*8.49*	*1.05*	*0.02*	*0.01*	*0.81*
30 at%	*0.77*	*2.20*	*8.81*	*-3.67*	*1.06*

Samples Annealed at 600 °C					
	2.5 um	**5 um**	**10 um**	**20 um**	**30 um**
0 at% (Ge)	*-51.97*	*0.05*	*0.05*	*0.08*	*-1.35*
15 at%	*0.07*	*0.07*	*0.09*	*0.10*	*0.07*
30 at%	*0.08*	*8.09*	*21.83*	*0.08*	*0.09*

Samples Annealed at 700 °C					
	2.5 um	**5 um**	**10 um**	**20 um**	**30 um**
0 at% (Ge)	*8.49*	*1.05*	*0.02*	*0.01*	*0.81*
15 at%	*13.65*	*-2.79*	*-0.74*	*0.23*	*0.19*
30 at%	*1.25*	*0.11*	*0.24*	*76.54*	*41.24*

measurements and remembering that amorphous Si (as well as amorphous SiGe) has no long-range order of the atoms. Both the XRD and Raman data acquired, along with that of other investigations[52,53], show only small changes in amorphous Si and Ge by annealing up until 600 °C and 400 °C, respectively, implying that the number and size of the microstructures are not changing but only undergoing small atomic and/or electronic rearrangements. This can also be observed in the reflectance measurements, particularly for that of Si. In this temperature range, the mobility of the atoms increase and are high enough for significant atom movement, but the number of gap states diminish as there is a decrease in the unpaired electrons in the amorphous structure ("dangling bonds"). This

also can explain the very slight decrease in conductivity for the higher Ge content sample since germanium requires a lower anneal time.

There is also an expected trend that conductivity increases with both increasing Ge content and increasing annealing temperature (as well as with each parameter individually, shown previously), though only once crystallization is reached, i.e. 700 °C samples have better conductivity than 600 °C but AD samples are better than 600 °C. With the higher Ge content samples ($x = 0.3$) the conductivity is comparable to or better than that of the AD samples. In relation to the photo response of the samples, there is little to no distinction between dark and photoconductivity, σ_L, for AD and 600 °C samples, which are on the order of 10^{-3} to 10^{-8}, respectively. With a higher anneal temperature of 700 °C there is observable conductivity from light illumination. I would expect the AD samples to exhibit little to no change between dark and photo-conductivity but expected at least a measurable difference in the 600 °C.

There must also be some expected variance in the results due to possible negative effects that need to be taken into consideration, such as micro-cracks occurring on the interface of the film and substrate due to thermal stress between them. It had been observed that one of the samples flaked very badly after deposition of Cr onto the SiGe surface. Although no other sample suffered such an outcome one must consider the possibility of poor adhesion therefore compromising the electrical measurements of the sample. One must also account for uncompensated oxidation on the surface, particularly for contact measurements and for etching. Precautions were taken to prevent such oxidation as much as possible, but was not able to be avoided all together.

Of the 12 samples under investigation there is only one data set and one data pair that does not produce results that are in agreement with the other data points. For the as-deposited Si data set there is a significant difference in measured resistivity between this sample and the rest. Also, there is one data pair on a sample that does not correspond well with the other data points. The outlying data set is marked in yellow while the data set with an outlying data point is marked in orange in Table 6.

Table 6 Resistivity of the samples of various compositions and anneal times for both dark and photo measurements. The as-deposited Si sample is highlighted because it does not correspond well with other samples. The 600 °C $Si_{.85}Ge_{.15}$ sample is marked orange because it contains an outlying data point.

		Dark		Photo	
		Mean	*Std. Dev.*	*Mean*	*Std. Dev.*
As-Dep.	*Si*	1.28×10^{-6}	8.01×10^{-7}	1.33×10^{-6}	8.73×10^{-7}
	$Si_{.85}Ge_{.15}$	2.16×10^{2}	7.62×10^{1}	2.10×10^{2}	6.65×10^{1}
	$Si_{.70}Ge_{.30}$	2.21×10^{2}	6.54×10^{1}	2.14×10^{2}	6.27×10^{1}
600 °C	*Si*	8.40×10^{5}	6.86×10^{5}	8.41×10^{5}	6.85×10^{5}
	$Si_{.85}Ge_{.15}$	8.63×10^{4}	5.79×10^{4}	8.62×10^{4}	5.78×10^{4}
	$Si_{.70}Ge_{.30}$	2.58×10^{2}	9.82×10^{1}	2.40×10^{2}	7.26×10^{1}
700 °C	*Si*	1.34×10^{2}	2.60×10^{1}	1.34×10^{2}	2.22×10^{1}
	$Si_{.85}Ge_{.15}$	1.04×10^{4}	6.84×10^{3}	1.03×10^{4}	7.00×10^{3}
	$Si_{.70}Ge_{.30}$	2.19×10^{2}	5.77×10^{1}	1.87×10^{2}	6.76×10^{1}

5. Conclusion and Outlook

In this chapter a summary of the thesis is given with an overview of the experiments and results. An outlook of future work is provided.

5.1 Conclusions

In this thesis, a study on structural and electrical properties for RF deposited $Si_{1-x}Ge_x$ polycrystalline alloy has been presented. A complete experimental setup that allows the repeatable production of $Si_{1-x}Ge_x$ alloy on 4 in. diameter was established. Sputtered thin film alloys were characterized utilizing several techniques and various equipment including macroscopic and microscopic examinations, both before and after annealing, to determine changes in crystal structure and electrical properties. I have examined the X-ray diffraction (XRD) spectra, Raman spectra, reflectance, and electrical conductivity of amorphous $Si_{1-x}Ge_x$ and polycrystalline $Si_{1-x}Ge_x$ thin films.

It has been shown that there is a non-negligible dependence of conductivity on composition, anneal temperature, and electrode spacing for the development of $Si_{1-x}Ge_x$ for device applications with a drop in conductivity at low anneal times due to a decrease in available states and despite an increase in mobility.

In conclusion, it has been shown that using a co-sputtering technique it is possible to easily prepare polycrystalline thin films by deposition of a-$Si_{1-x}Ge_x$ thin film alloys with various compositions with the structural and electronic properties of these films are comparable to those prepared by similar methods.

5.2 Outlook

The development of a SiGe based NIR optical sensor is very feasible due to the enticing characteristics of the alloy. As has been shown, the semiconductor alloy structure can be modified through annealing and its optical and thermal properties tailored by modifying anneal time and temperature, composition, and electrode spacing. A more in depth study on the effects of high anneal temp/time and high Ge content along with variation in deposition parameters can yield very favorable results.

Bibliography

1 T. D. Moustakas, D. A. Anderson, and W. Paul, "PREPARATION OF HIGHLY PHOTOCONDUCTIVE AMORPHOUS SILICON BY RF SPUTTERING," Solid State Commun. **23** (3), 155-158 (1977).

2 M. H. Brodsky, R. S. Title, K. Weiser, and G. D. Pettit, "STRUCTURAL, OPTICAL, AND ELECTRICAL PROPERTIES OF AMORPHOUS SILICON FILMS," Physical Review B **1** (6), 2632-& (1970).

3 R. Grigorov, "Amorphous Germanium and Silicon (Structure Andtransport Phenomena)," Mater. Res. Bull. **3** (1), 13-& (1968).

4 J. Tauc, "OPTICAL PROPERTIES AND ELECTRONIC STRUCTURE OF AMORPHOUS," Mater. Res. Bull. **3** (1), 37-& (1968).

5 P. A. Walley, "Electrical Conduction in Amorphous Silicon and Germanium," Thin Solid Films **2** (4), 327-& (1968).

6 A. H. Clark, "Electrical and Optical Properties of Amorphous Germanium," Phys Rev **154** (3), 750-& (1967).

7 A. Axelevitch and G. Golan, "Novel silicon high sensitive photonic sensor," Microelectron. J. **40** (3), 435-438 (2009).

8 A. Rogalski, "Infrared detectors: status and trends," Prog. Quantum Electron. **27** (2-3), 59-210 (2003).

9 Y. K. Fang, S. B. Hwang, K. H. Chen, C. R. Liu, and L. C. Kuo, "A METAL AMORPHOUS-SILICON GERMANIUM ALLOY SCHOTTKY-BARRIER FOR INFRARED OPTOELECTRONIC IC ON GLASS SUBSTRATE APPLICATION," IEEE Trans. Electron Devices **39** (6), 1350-1354 (1992).

10 R. Roucka, J. Xie, J. Kouvetakis, J. Mathews, V. D'Costa, J. Menendez, J. Tolle, and S. Q. Yu, "Ge1-ySny photoconductor structures at 1.55 mu m: From advanced materials to prototype devices," J Vac Sci Technol B **26** (6), 1952-1959 (2008).

11 G. Masini, L. Colace, F. Petulla, G. Assanto, V. Cencelli, and F. DeNotaristefani, "Monolithic and hybrid near infrared detection and imaging based on poly-Ge photodiode arrays," Opt. Mater. **27** (5), 1079-1083 (2005).

12 D. Bahloul-Hourlier and P. Perrot, "Thermodynamics of the Au-Si-O system: Application to the synthesis and growth of silicon-silicon dioxide nanowires," J. Phase Equilib. Diffus. **28** (2), 150-157 (2007).

13 D. C. Miller, C. F. Herrmann, H. J. Maier, S. M. George, C. R. Stoldt, and K. Gall, "Thermo-mechanical evolution of multilayer thin films: Part II. Microstructure evolution in Au/Cr/Si micro cantilevers," Thin Solid Films **515** (6), 3224-3240 (2007).

14 K. Tajima, F. Qiu, W. Shin, N. Sawaguchi, N. Izu, I. Matsubara, and N. Murayama, "Thermoelectric properties of RF-sputtered SiGe thin film for hydrogen gas sensor," Japanese journal of applied physics **43** (no. 9 a), 5978-5983 (2004).

15 Y. W. Su and H. L. Hwang, "A Comparison between Different Structures of Amorphous-Silicon Image Sensors," Thin Solid Films **202** (2), 181-189 (1991).

16 Q. S. Lei, H. X. Xu, and J. P. Xu, "DEVELOPMENT OF HIGHLY CONDUCTIVE P-TYPE MICROCRYSTALLINE SILICON FILMS FOR N-I-P FLEXIBLE SOLAR CELLS APPLICATION," International Journal of Modern Physics B **24** (28), 5527-5538 (2010).

17 H. D. Goldbach, A. Bink, and R. E. I. Schropp, "Thin p(++) mu c-Si layers for use as back surface field in p-type silicon heterojunction solar cells," J. Non-Cryst. Solids **352** (9-20), 1872-1875 (2006).

18 M. A. Martinez, C. Guillen, A. Morales, and J. Herrero, "Arrangement of flexible foil substrates for CuInSe2-based solar cells," Surf. Coat. Technol. **148** (1), 61-64 (2001).

19 Y. Hamakawa, K. Fujimoto, K. Okuda, Y. Kashima, S. Nonomura, and H. Okamoto, "NEW TYPES OF HIGH-EFFICIENCY SOLAR-CELLS BASED ON A-SI," Appl Phys Lett **43** (7), 644-646 (1983).

20 V. Suendo, G. Patriarche, and P. Roca i Cabarrocas, "Influence of deposition parameters and post-deposition plasma treatments on the photoluminescence of polymorphous silicon carbon alloys," J. Non-Cryst. Solids **352** (9-20), 1357-1360 (2006).

21 C. D. Abel, T. Toyama, T. Matsui, H. Okamoto, and Y. Hamakawa, "Effect of free carriers on ac-driven electroluminescent devices with hydrogenated amorphous silicon carbide thin films," Jpn J Appl Phys 1 **35** (10), 5288-5292 (1996).

22 H. Munekata and H. Kukimoto, "ELECTRO-LUMINESCENCE IN HYDROGENATED AMORPHOUS SILICON-CARBON ALLOY," Appl Phys Lett **42** (5), 432-434 (1983).

23 M. Yildiz, S. Dost, and B. Lent, "Growth of bulk SiGe single crystals by liquid phase diffusion," J Cryst Growth **280** (1-2), 151-160 (2005).

24 M. Yildiz and S. Dost, "A continuum model for the Liquid Phase Diffusion growth of bulk SiGe single crystals," Int J Eng Sci **43** (13-14), 1059-1080 (2005).

25 Niels Bohr, "On the Constitution of Atoms and Molecules, Part I", in *Philosophical Magazine* (1913), Vol. 26, pp. 1-24.

26 Niels Bohr, "On the Constitution of Atoms and Molecules, Part II Systems Containing Only a Single Nucleus", in *Philosophical Magazine* (1913), Vol. 26, pp. 476-502.

27 R. Braunstein, A. R. Moore, and F. Herman, "Intrinsic optical absorption in Ge-Si alloys," Phys Rev **109**, 695 (1958).

28 Y. P. Varshni, "TEMPERATURE DEPENDENCE OF ENERGY GAP IN SEMICONDUCTORS," Physica **34** (1), 149-& (1967).

29 E. R. Johnson and S. M. Christian, "Some Properties of Germanium-Silicon Alloys," Phys Rev **95** (2), 560-561 (1954).

30 J. Weber and M. I. Alonso, "Near-Band-Gap Photoluminescence of Si-Ge Alloys," Physical Review B **40** (8), 5683-5693 (1989).

31 G. L. Pearson and J. Bardeen, "ELECTRICAL PROPERTIES OF PURE SILICON AND SILICON ALLOYS CONTAINING BORON AND PHOSPHORUS," Phys Rev **75** (5), 865-883 (1949).

32 H. Brooks, Adv. Electron. Electron Phys **7**, 85 (1955).

33 F. A. Kroger, Chemistry Imperfect, 252 (1964).

34 C. D. Thurmond, "The Standard Thermodynamic Functions for the Formation of Electrons and Holes in Ge, Si, GaAs, and GaP," Journal of The Electrochemical Society **122** (8), 1133-1141 (1975).

35 H. R. Philipp and E. A. Taft, "Optical Constants of Germanium in the Region-1 to 10 Ev," Phys Rev **113** (4), 1002-1005 (1959).

36 W. W. Hernandez-Montero, I. E. Zaldivar-Huerta, C. Zuniga-Islas, A. Torres-Jacome, C. Reyes-Betanzo, and A. Itzmoyotl-Toxqui, "Optical and compositional properties of amorphous silicon-germanium films by plasma processing for integrated photonics," Opt. Mater. Express **2** (4), 358-370 (2012).

37 J. Humlicek, *Properties of Strained and Relaxed Silicon Germanium*. (ISPEC, IEE, London, UK, 1988).

38 A. Roeseler J. Humlicek, T. Zettler, M. G. Kekoua, E. Khoutsishvili, Appl. Opt. **31**, 90 (1992).

39 K. Zellama, P. Germain, S. Squelard, J. C. Bourgoin, and P. A. Thomas, "CRYSTALLIZATION IN AMORPHOUS-SILICON," J. Appl. Phys. **50** (11), 6995-7000 (1979).

40 P. Germain, K. Zellama, S. Squelard, J. C. Bourgoin, and A. Gheorghiu, "CRYSTALLIZATION IN AMORPHOUS-GERMANIUM," J. Appl. Phys. **50** (11), 6986-6994 (1979).

41 N. A. Blum and C. Feldman, "CRYSTALLIZATION KINETICS OF AMORPHOUS-GERMANIUM AND SILICON FILMS," Bulletin of the American Physical Society **21** (3), 334-334 (1976).

42 Jung Won Park, University of Tennessee, 2009.

43 E.V. Jelenkovic, KY Tong, Z. Sun, CL Mak, and WY Cheung, "Properties of crystallized SiGe thin films deposited by sputtering," Journal of Vacuum Science & Technology A: Vacuum, Surfaces, and Films **15**, 2836 (1997).

44 LK Teh, WK Choi, LK Bera, and WK Chim, "Structural characterisation of polycrystalline SiGe thin film," Solid State Electron **45** (11), 1963-1966 (2001).

45 J. P. Dismukes, R. J. Paff, and L. Ekstrom, "Lattice Parameter + Density in Germanium-Silicon Alloys," J Phys Chem-Us **68** (10), 3021-& (1964).

46 N. Vandong, T. H. Danh, and J. Y. Leny, "DARK CONDUCTIVITY AND PHOTOCONDUCTIVITY OF HYDROGENATED AMORPHOUS SI1-XGEX ALLOYS," J. Appl. Phys. **52** (1), 338-341 (1981).

47 A. K. Ghosh, T. McMahon, E. Rock, and H. Wiesmann, "OPTICAL AND ELECTRICAL-PROPERTIES OF EVAPORATED AMORPHOUS SILICON WITH HYDROGEN," J. Appl. Phys. **50** (5), 3407-3413 (1979).

48 M. Serenyi, J. Betko, A. Nemesics, N. Q. Khanh, D. K. Basa, and M. Morvic, "Study on the RF Sputtered hydrogenated amorphous silicon-germanium thin films," Microelectron. Reliab. **45** (7-8), 1252-1256 (2005).

49 S. Z. Weisz, Y. Goldstein, M. Gomez, J. A. Muir, O. Resto, and R. Perez, "THE COMPOSITIONAL DEPENDENCE OF THE OPTICAL AND ELECTRICAL-

PROPERTIES OF HYDROGENATED AMORPHOUS SI-GE FILMS PREPARED BY CO-SPUTTERING," Thin Solid Films **119** (1), 59-65 (1984).

50 P. K. Banerjee, R. Dutta, S. S. Mitra, and D. K. Paul, "PROPERTIES OF RF SPUTTERED HYDROGENATED AMORPHOUS GERMANIUM-SILICON ALLOYS," J. Non-Cryst. Solids **50** (1), 1-11 (1982).

51 Moshe Weizman, Berlin, Techn. University, 2008.

52 S. C. Moss and J. F. Graczyk, "EVIDENCE OF VOIDS WITHIN AS-DEPOSITED STRUCTURE OF GLASSY SILICON," Phys. Rev. Lett. **23** (20), 1167-& (1969).

53 G Breitling, "SOLID AMORPHOUS GE AND AS AS EXAMPLES OF LATTICE-LIKE AMORPHOUS SUBSTANCES," Journal of Vacuum Science & Technology **6** (4), 628-& (1969).

Appendix

This thesis has measured, calculated, or observed basic physical properties of the $Si_{1-x}Ge_x$ alloy but is by no means exhaustive. The information is summarized and presented in table format below.

Table 7 Presented here is a summary of several of the basic physical properties of Si, Ge, and the $Si_{1-x}Ge_x$ alloy at the compositions used throughout this thesis.

Properties	Ge	$Si_{.70}Ge_{.30}$	$Si_{.85}Ge_{.15}$	Si
Atoms / cm^3	4.42×10^{22}	4.83×10^{22}	4.91×10^{22}	5.0×10^{22}
Atomic weight	72.60	41.44	34.77	28.09
Crystal Structure	Diamond Cubic	Diamond Cubic	Diamond Cubic	Diamond Cubic
Density (g/cm^3)	5.3267	3.228	2.778	2.328
Indirect Energy Gap at 300 K (eV)	0.66	1.03	1.09	1.12
Intrinsic Resistivity (Ω-cm)	47	1.6×10^5	1.96×10^5	2.3×10^5
Lattice Constant (nm)	0.56575	0.54932	0.54615	0.54311
Melting Temperature (°C)	938	1271	1343	1414
Specific Heat (J/g-°C)	0.31	0.58	0.64	0.7

Vita

Daniel Schaeffer earned his Bachelors of Science in physics from Brigham Young University – Idaho with minors in applied mathematics and computer science before attending the University of Tennessee. Along with being a graduate student, he works at Oak Ridge National Laboratory (ORNL) in the Measurement Sciences and Systems Engineering Division. Among others, his research includes nanomaterials and superhydrophobic coatings. He plans to continue his education in pursuit of a Ph.D while continuing to work at ORNL. During his free time, Daniel enjoys playing sports, playing the piano, and participating in outdoor activities.